



Calhoun: The NPS Institutional Archive
DSpace Repository

Theses and Dissertations

1. Thesis and Dissertation Collection, all items

2013-06

Integration of twenty-bladed cross-flow fan into vertical take-off and landing aircraft

Jones, Andria M.

Monterey, California: Naval Postgraduate School

<http://hdl.handle.net/10945/34682>

Downloaded from NPS Archive: Calhoun



Calhoun is a project of the Dudley Knox Library at NPS, furthering the precepts and goals of open government and government transparency. All information contained herein has been approved for release by the NPS Public Affairs Officer.

Dudley Knox Library / Naval Postgraduate School
411 Dyer Road / 1 University Circle
Monterey, California USA 93943

<http://www.nps.edu/library>



**NAVAL
POSTGRADUATE
SCHOOL**

MONTEREY, CALIFORNIA

THESIS

**INTEGRATION OF TWENTY-BLADED CROSS-FLOW FAN
INTO VERTICAL TAKE-OFF AND LANDING AIRCRAFT**

by

Andria M. Jones

June 2013

Thesis Advisor:
Second Reader:

Garth V. Hobson
Anthony J. Gannon

Approved for public release; distribution is unlimited

THIS PAGE INTENTIONALLY LEFT BLANK

REPORT DOCUMENTATION PAGE			<i>Form Approved OMB No. 0704-0188</i>
Public reporting burden for this collection of information is estimated to average 1 hour per response, including the time for reviewing instruction, searching existing data sources, gathering and maintaining the data needed, and completing and reviewing the collection of information. Send comments regarding this burden estimate or any other aspect of this collection of information, including suggestions for reducing this burden, to Washington headquarters Services, Directorate for Information Operations and Reports, 1215 Jefferson Davis Highway, Suite 1204, Arlington, VA 22202-4302, and to the Office of Management and Budget, Paperwork Reduction Project (0704-0188) Washington, DC 20503.			
1. AGENCY USE ONLY (Leave blank)	2. REPORT DATE June 2013	3. REPORT TYPE AND DATES COVERED Master's Thesis	
4. TITLE AND SUBTITLE INTEGRATION OF TWENTY-BLADED CROSS-FLOW FAN INTO VERTICAL TAKE-OFF AND LANDING AIRCRAFT		5. FUNDING NUMBERS TDSI/11-007/1A - NPS	
6. AUTHOR(S) Andria M. Jones			
7. PERFORMING ORGANIZATION NAME(S) AND ADDRESS(ES) Naval Postgraduate School Monterey, CA 93943-5000		8. PERFORMING ORGANIZATION REPORT NUMBER	
9. SPONSORING /MONITORING AGENCY NAME(S) AND ADDRESS(ES) TDSI - National University of Singapore 21 Lower Kent Ridge Road Singapore, 119077		10. SPONSORING/MONITORING AGENCY REPORT NUMBER	
11. SUPPLEMENTARY NOTES The views expressed in this thesis are those of the author and do not reflect the official policy or position of the Department of Defense or the U.S. Government. IRB Protocol number ____N/A____.			
12a. DISTRIBUTION / AVAILABILITY STATEMENT Approved for public release; distribution is unlimited		12b. DISTRIBUTION CODE	
13. ABSTRACT (maximum 200 words) The research presented is dedicated to determining an efficient rotor and housing system that will generate a sufficient thrust-to-weight ratio for vertical take-off and landing through computational modeling, implementation and experimentation. To accomplish this task, a new 20-bladed rotor was designed in SolidWorks and imported into ANSYS-CFX, which was used to analytically determine the thrust generated at speeds ranging from 4,000 rpm to 10,000 rpm. Upon successful simulation, a carbon-fiber model was fabricated and tested at speeds from 4,000 rpm to 9,700 rpm. With a promising thrust-to-weight ratio, a platform was built for initial testing utilizing two motors and four cross-flow fans. Initial platform testing was successful and generated sufficient thrust for vertical take-off.			
14. SUBJECT TERMS Vertical take-off, VTOL, cross-flow fan, CFF			15. NUMBER OF PAGES 89
			16. PRICE CODE
17. SECURITY CLASSIFICATION OF REPORT Unclassified	18. SECURITY CLASSIFICATION OF THIS PAGE Unclassified	19. SECURITY CLASSIFICATION OF ABSTRACT Unclassified	20. LIMITATION OF ABSTRACT UU

THIS PAGE INTENTIONALLY LEFT BLANK

Approved for public release; distribution is unlimited

**INTEGRATION OF TWENTY-BLADED CROSS-FLOW FAN INTO VERTICAL
TAKE-OFF AND LANDING AIRCRAFT**

Andria M. Jones
Lieutenant, United States Navy
B.S., United States Naval Academy, 2006

Submitted in partial fulfillment of the
requirements for the degree of

MASTER OF SCIENCE IN MECHANICAL ENGINEERING

from the

**NAVAL POSTGRADUATE SCHOOL
June 2013**

Author: Andria M. Jones

Approved by: Garth V. Hobson
Thesis Advisor

Anthony J. Gannon
Second Reader

Knox T. Millsaps
Chair, Department of Mechanical and Aerospace Engineering

THIS PAGE INTENTIONALLY LEFT BLANK

ABSTRACT

The research presented is dedicated to determining an efficient rotor and housing system that will generate a sufficient thrust-to-weight ratio for vertical take-off and landing through computational modeling, implementation and experimentation. To accomplish this task, a new 20-bladed rotor was designed in SolidWorks and imported into ANSYS-CFX, which was used to analytically determine the thrust generated at speeds ranging from 4,000 rpm to 10,000 rpm. Upon successful simulation, a carbon-fiber model was fabricated and tested at speeds from 4,000 rpm to 9,700 rpm. With a promising thrust-to-weight ratio, a platform was built for initial testing utilizing two motors and four cross-flow fans. Initial platform testing was successful and generated sufficient thrust for vertical take-off.

THIS PAGE INTENTIONALLY LEFT BLANK

TABLE OF CONTENTS

I	INTRODUCTION.....	1
A.	OVERVIEW	1
B.	BACKGROUND	1
C.	OBJECTIVES	6
II.	DESIGN AND SIMULATION	7
A.	DESIGN OVERVIEW.....	7
B.	SIMULATION OVERVIEW.....	8
1.	Rendering.....	8
2.	Mesh Generation.....	9
3.	Setup.....	11
4.	ANSYS-CFX CFD Analysis	13
III.	EXPERIMENTAL SETUP	15
A.	SOLIDWORKS DESIGN	15
B.	FABRICATION	15
1.	Material Selection	15
2.	Design and Construction	16
3.	Motor Selection	17
C.	EQUIPMENT SETUP	18
1.	Cross-flow Fan Assembly	18
2.	Test Platform.....	19
3.	Cross-flow Fan Control	20
4.	Instrumentation.....	21
5.	Data Acquisition.....	22
IV.	RESULTS AND DISCUSSION	25
1.	Thrust.....	30
2.	Velocity Profiles	32
3.	Power.....	34
V.	DESIGN, FABRICATION, AND TESTING OF FLYING PLATFORM	37
1.	Experimental Setup	40
2.	Platform Control.....	40
3.	Platform Testing.....	41
VI.	CONCLUSIONS AND RECOMMENDATIONS.....	43
APPENDIX A.	ANSYS-CFX SETTINGS AT 9,000 RPM	45
APPENDIX B.	SCORPION MOTOR SPECIFICATIONS	49
APPENDIX C.	ANALYTICAL DATA	53
APPENDIX D.	ANSYS-CFX FLOW FIELDS AT ALL SPEEDS	55
APPENDIX E.	ANSYS-CFX STREAM LINES AT ALL SPEEDS.....	61

APPENDIX F. EXPERIMENTAL TEST DATA	67
LIST OF REFERENCES.....	69
INITIAL DISTRIBUTION LIST	71

LIST OF FIGURES

Figure 1.	Cross-flow fan diagram. From [1].	2
Figure 2.	Technotech Enterprises Commercial cross-flow fan.	2
Figure 3.	Example of cross-flow fan housing. From [2].	3
Figure 4.	Propulsive Wing aircraft. From [13].	5
Figure 5.	Cross-section of Propulsive Wing aircraft. From [13].	5
Figure 6.	Boundary layer separation of Propulsive Wing aircraft. From [13].	5
Figure 7.	SolidWorks 20-bladed rotor model.	7
Figure 8.	SolidWorks housing model. From [14].	8
Figure 9.	Named sections of rotor and housing.	9
Figure 10.	Two-dimensional mesh with 850,732 nodes.	10
Figure 11.	Close-up of rotor blade mesh with a single element thickness.	11
Figure 12.	SolidWorks 20-bladed cross-flow fan assembly.	15
Figure 13.	SolidWorks model for upper portion of housing mold.	16
Figure 14.	SolidWorks model for lower portion of housing mold.	16
Figure 15.	Custom wood carbon-fiber molds for the cross-flow fan housing.	17
Figure 16.	Scorpion Motors 4025, 4035, and 5035, respectively. From [17].	18
Figure 17.	Thunder Power RC lithium polymer battery.	18
Figure 18.	Test platform and cross-flow fan assembly.	19
Figure 19.	Triple-beam balance used for measuring thrust.	19
Figure 20.	Digital balance used for thrust measurement.	20
Figure 21.	Scorpion motor potentiometer.	20
Figure 22.	Potentiometer motor control assembly.	21
Figure 23.	Strobe tachometer used to measure speed.	21
Figure 24.	Fluke multimeter used to measure voltage.	22
Figure 25.	Clip on ammeter used to measure current.	22
Figure 26.	Experimental setup with router.	23
Figure 27.	Conservation of mass verification at 9,000 rpm.	25
Figure 28.	Torque convergence at 9,000 rpm.	26
Figure 29.	K-epsilon turbulence model flow visualization at 9,000 rpm.	27
Figure 30.	Laminar flow model visualization at 9,000 rpm.	27
Figure 31.	Close-up of k-epsilon flow field at 9,000 rpm showing vectors and vortices.	28
Figure 32.	Close-up of k-epsilon recirculation flow in outlet at 9,000 rpm.	28
Figure 33.	Streamlines at 9,000 rpm with the k-epsilon turbulence model.	29
Figure 34.	Laminar flow model streamlines at 9,000 rpm.	30
Figure 35.	Analytical and experimental thrust comparison.	31
Figure 36.	K-epsilon velocity profile at 9,000 rpm.	33
Figure 37.	Laminar model velocity profile at 9,000 rpm.	33
Figure 38.	Analytical and experimental power comparison.	35
Figure 39.	SolidWorks platform design.	38
Figure 40.	Aluminum carbon-fiber mold for test platform.	39
Figure 41.	Assembled platform with four cross-flow fans and two motors.	40

Figure 42.	Successful lift-off of four rotor chassis.....	41
Figure 43.	Flow Field at 4,000 rpm with the k-epsilon turbulence model.....	55
Figure 44.	Flow Field at 6,000 rpm with the k-epsilon turbulence model.....	55
Figure 45.	Flow Field at 8,000 rpm with the k-epsilon turbulence model.....	56
Figure 46.	Flow Field at 9,000 rpm with the k-epsilon turbulence model.....	56
Figure 47.	Flow Field at 9,500 rpm with the k-epsilon turbulence model.....	57
Figure 48.	Flow Field at 10,000 rpm with the k-epsilon turbulence model.....	57
Figure 49.	Laminar flow field at 4,000 rpm.....	58
Figure 50.	Laminar flow field at 6,000 rpm.....	58
Figure 51.	Laminar flow field at 8,000 rpm.....	59
Figure 52.	Laminar flow field at 9,000 rpm.....	59
Figure 53.	Laminar flow field at 10,000 rpm.....	60
Figure 54.	Streamlines at 4,000 rpm with the k-epsilon turbulence model.....	61
Figure 55.	Streamlines at 6,000 rpm with the k-epsilon turbulence model.....	61
Figure 56.	Streamlines at 8,000 rpm with the k-epsilon turbulence model.....	62
Figure 57.	Streamlines at 9,000 rpm with the k-epsilon turbulence model.....	62
Figure 58.	Streamlines at 9,500 rpm with the k-epsilon turbulence model.....	63
Figure 59.	Streamlines at 10,000 rpm with the k-epsilon turbulence model.....	63
Figure 60.	Laminar flow streamlines at 4,000 rpm.....	64
Figure 61.	Laminar flow streamlines at 6,000 rpm.....	64
Figure 62.	Laminar flow streamlines at 8,000 rpm.....	65
Figure 63.	Laminar flow streamlines at 9,000 rpm.....	65
Figure 64.	Laminar flow streamlines at 10,000 rpm.....	66

LIST OF TABLES

Table 1.	ANSYS-CFX settings for various speeds.	12
Table 2.	Experimental thrust values.....	31
Table 3.	Thrust values determined analytically via ANSYS-CFX.	32
Table 4.	Experimental power.	36
Table 5.	Analytical Power.....	36
Table 6.	Weight of cross-flow-fan assembly with possible motors.....	37
Table 7.	Thrust-to-weight ratios for each motor.	38

THIS PAGE INTENTIONALLY LEFT BLANK

LIST OF ACRONYMS AND ABBREVIATIONS

A	Area [m ²]
a _i	Elemental area [m ²]
CFX-Pre	Part of the ANSYS-CFX package for application of boundary and initial conditions as well as solver settings
CFD	Computational fluid dynamics
CFF	Cross-flow fan
DC	Direct current
	Turbulent dissipation [m ² /s ³]
	Non-dimensional total pressure correction term [1]
h	Specific enthalpy [kJ/kg]
I	Current [A]
ID	Inside diameter [m]
k	Turbulent kinetic energy [J]
	Thermal conductivity [W/(m·K)]
LTV	Ling-Temco-Vought
OD	Outside diameter [m]
P	Power [kW]
p	Pressure [Pa]
p _o	Total Pressure [Pa]
	Density [kg/m ³]
RC	Remote control
rpm	Revolutions per minute
S _E	Energy source equation

S_M	Momentum source equation
SolidWorks	Three-dimensional drafting and solid modeling software package
T	Temperature [K]
TPL	Turbopropulsion Laboratory
T_t	Total temperature [K]
μ	Dynamic viscosity [Pa·s]
μ_t	Turbulent viscosity [Pa·s]
U	Velocity [m/s]
UAV	Unmanned Aerial Vehicle(s)
V	Voltage [V]
VTOL	Vertical take-off and landing
	Torque [Nm]
	Rotational Speed [rad/s]

ACKNOWLEDGMENTS

I would like to express my gratitude and appreciation to the following people:

Mohammad Kohistany, for his never-ending support of me in accomplishing this research.

Bradley Kohistany, for his inspiration.

Christopher Clay, for his enthusiasm and in-depth knowledge of machining and design, as well as the many hours he dedicated to fabrication of the cross-flow fans and experimental platform.

Professor Garth Hobson, for his in-depth knowledge of fluid dynamics, genuine interest, and guidance throughout the research.

Professor Anthony Gannon, for his assistance in every aspect of CFD computation and analysis.

John Gibson, for his assistance and constant support during the testing and design phase of this research.

Mike McCormick, for his thorough knowledge of hamming and assistance in creating a successful mesh.

Scott Drayton, for his professional and academic guidance while taking classes at NPS and conducting research at the Turbopropulsion Laboratory.

Joe Keller, for his professional guidance and leadership while taking classes at the Naval Postgraduate School.

THIS PAGE INTENTIONALLY LEFT BLANK

I INTRODUCTION

A. OVERVIEW

With the evolution of society, warfare, and the ever-increasing need for flexibility, there is a renewed interest in designing a fixed-wing aircraft capable of Vertical Take-Off and Landing (VTOL). A vehicle that has the speed and range of a fixed-wing without the dangers associated with rotary-wing aircraft would be ideal for both civilian and military operations. The VTOL aircraft of today have complicated propulsion systems (Harrier) or are not completely fixed wing (Tiltrotor). One proposed solution is the integration of cross-flow fan technology as a propulsion system. This would allow for vertical take-off and transition utilizing thrust vectoring without the need for repositioning the rotor itself. Such a propulsion system would not only be safer but also allow for more flexibility in the design.

Cross-flow fans have many advantages. They are unique in that the flow travels transversely through the fan, thus passing the blades twice from the inlet to the outlet. Compared to conventional fans, they are more compact, provide high-pressure coefficients, lift coefficients, and thrust. Additionally, their large length-to-diameter ratio makes them essentially two-dimensional, which is optimal for integration into the wing of an aircraft.

B. BACKGROUND

The first successful cross-flow fan shown in Figure 1 was patented in 1893 by Paul Mortier (U.S. Pat No. 507,445) [1]. Since its introduction, it has been widely utilized for heating and cooling systems, ranging from households and commercial properties to computer cooling systems. An example of a typical commercial cross-flow fan is displayed in Figure 2.

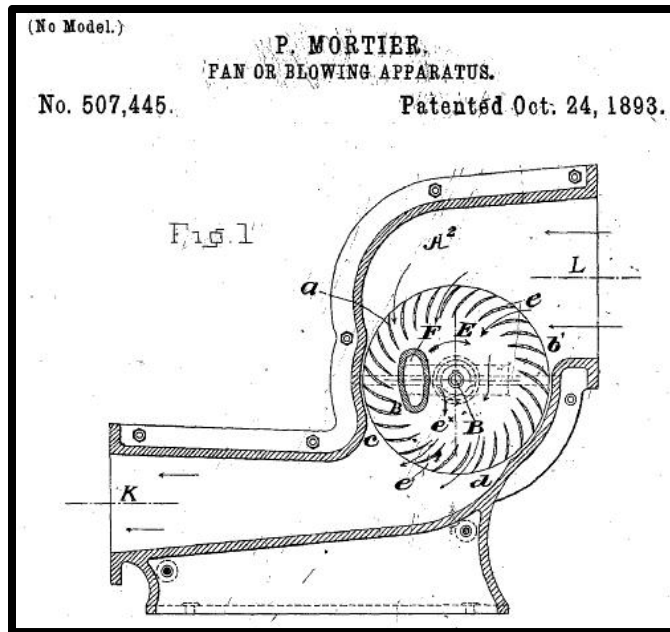


Figure 1. Cross-flow fan diagram. From [1].



Figure 2. Technotech Enterprises Commercial cross-flow fan.

In 1975, Naval Air Systems Command [2] recognized the potential of cross-flow fan technology and awarded a 12-month contract to Vought Systems Division to verify the performance of a multi-bypass ratio propulsion system. They designed and tested 12-inch diameter, 30-bladed cross-flow fans such as the one in Figure 3. Using spans of 1.5 inches and 12 inches, the cross-flow fans were tested at speeds from 6,000 rpm to 13,000 rpm. They varied the housing dimensions, and after a year of testing concluded

that the optimal design parameters were too complex to be determined during the course of the testing.

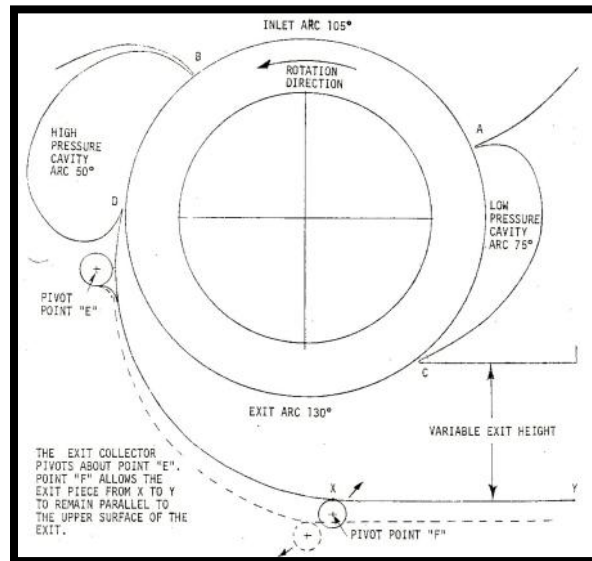


Figure 3. Example of cross-flow fan housing. From [2].

The next large-scale investigation took place at the University of Texas at Arlington. There, Harloff [3] used finite-element modeling to study cross-flow fan characteristics in 1979. Chawla [4] followed by working on the housing optimization of a cross-flow fan for integration into an airplane wing in 1984. Then Lin [5] investigated the external aerodynamics of an airfoil with an internal cross-flow fan in 1986. In 1988, Nieh [6] continued the research by conducting studies of the propulsive characteristics of a cross-flow fan installed in an airfoil.

Harloff continued research to test cross-flow fans at speeds up to 12,500 rpm and Chawla focused her research on the use of cross-flow fans for boundary layer control [6]. Chawla's research determined that not only were cross-flow fans effective for boundary layer control, but that the maximum lift coefficient could be increased to delay stall. They could not, however, generate a sufficient thrust-to-weight ratio for take-off.

Much research in cross-flow fan technology for propulsion was discontinued until the early 21st century. With a growing concern for highway and city traffic congestion, NASA began its "highway in the sky" initiative. The future of transportation

infrastructure was thought to be small piloted aircraft that could navigate the airways while relieving congestion problems on the ground. In coordination with NASA, the Naval Postgraduate School Turbopropulsion Laboratory reopened the investigation into cross-flow fan technology for VTOL aircraft in 2000.

The majority of research that followed focused on determining the most efficient rotor and housing design to generate a high enough thrust-to-weight ratio for VTOL. Gossett [7] began by proposing the integration of a cross-flow fan into a single seat VTOL aircraft for thrust augmentation. Cheng [8] continued the cross-flow fan research in 2003. He validated Vought Systems Division's research of a 12 inch diameter, 1.5 inch span cross-flow fan, and developed a baseline computational model for improving cross-flow fan design. Later, Schreiber [9] and Ulvin [10] studied the effect of variable span on a smaller 6 inch cross-flow fan. Then, Antoniadis [11] varied the number of blades and determined that 22 blades generated a higher thrust-to-weight ratio at all tested speeds than the 30-bladed rotor used previously.

Kummer and Allred [12] were the first to get their design off the ground. Although their vehicle, shown in Figure 4, is currently a short take-off and landing aircraft (STOL), it has paved the way for the future. They patented their cross-flow fan [13] propulsive system in 2010 after successfully demonstrating the advantages of such a vehicle at the University of Syracuse in New York. As seen in Figure 5, its large thickness-to-chord ratio allows it to not only carry three times the payload of conventional fixed wing aircraft, but also ten times the volume for its size and weight. Figure 6 demonstrates how their cross-flow fan design significantly reduces boundary layer separation, while increasing lift and decreasing the opportunity for stall.



Figure 4. Propulsive Wing aircraft. From [13].

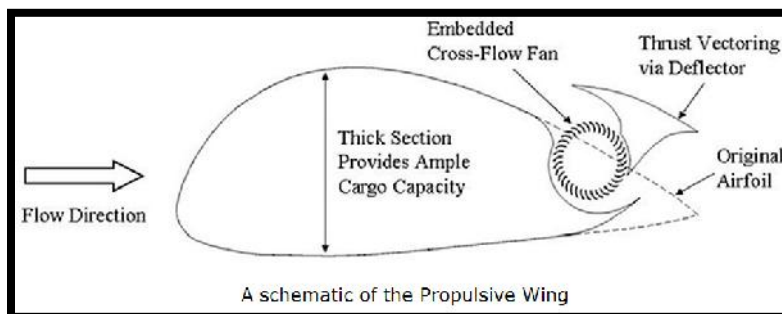


Figure 5. Cross-section of Propulsive Wing aircraft. From [13].

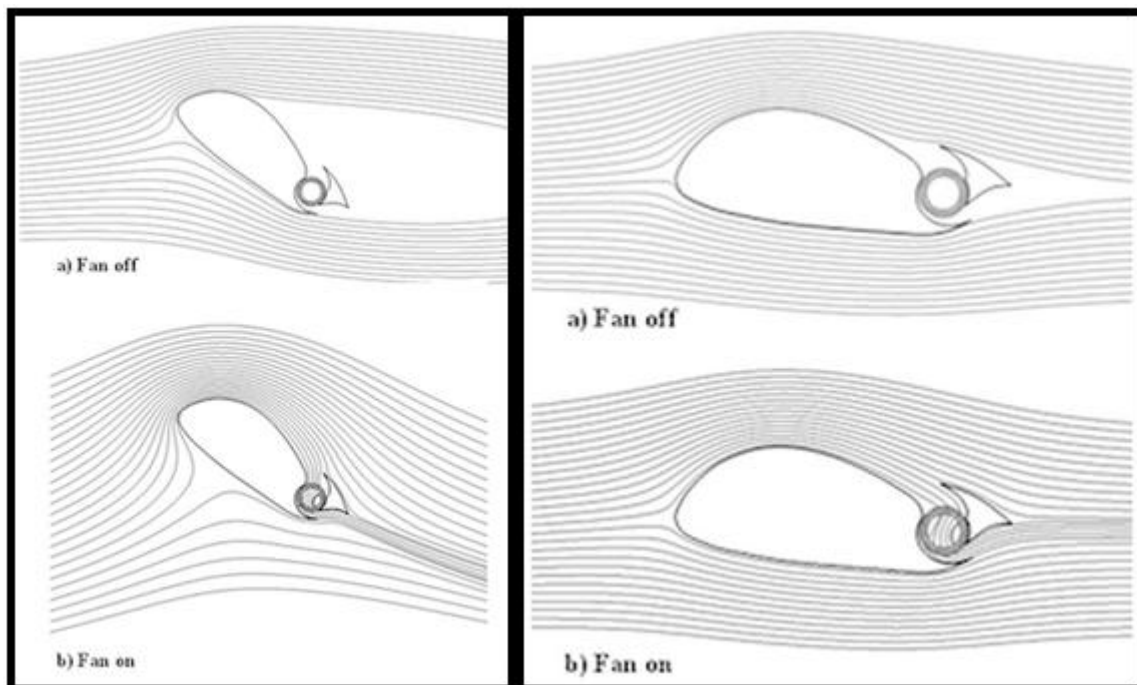


Figure 6. Boundary layer separation of Propulsive Wing aircraft. From [13].

The most recent research was conducted at the Naval Postgraduate School. Delagrange [14] used CFD analysis to design the optimum housing for a 78 mm diameter, 16-bladed cross-flow fan. Upon determining optimal housing, he constructed a steel housing and utilized a commercial carbon fiber rotor to validate CFD results through experimentation. Yeo's [15] work followed, using the optimal housing from Delagrange's research, he tested the thrust augmentation of a dual cross-flow fan setup to determine the prime spacing of a two rotor setup.

C. OBJECTIVES

The objective of this research is to design a cross-flow fan propulsion system capable of providing a thrust-to-weight ratio greater than 1.0. This would generate sufficient thrust for vertical take-off and landing. This includes the design, modelling, construction, and testing of a 20-bladed cross-flow fan with a 78 mm (3 in) diameter. Upon successful design with SolidWorks and simulation with ANSYS-CFX, the rotor and housing will be constructed from carbon fiber and tested experimentally in conjunction with the commercial Scorpion 4025 motor for validation. With promising results, the rotor and housing unit will then be integrated into a platform for vertical take-off and landing experimentation.

II. DESIGN AND SIMULATION

A. DESIGN OVERVIEW

The 20-bladed rotor design was selected for this analysis based on successful experimentation with Delagrange's [14] 16-bladed rotor. The 20-bladed rotor was created in SolidWorks with 11.08 mm chord length blade profiles and can be seen in Figure 7. The housing used was a slightly modified version of the housing that was optimized by Delagrange [14] and is shown in Figure 8. An outer rotor domain diameter of 80 mm allowed for a 1 mm clearance between the housing and rotor domains. When imported into ANSYS-CFX this created a total clearance of 2 mm between the housing walls and blade tips of the rotor. The thickness of both rotor and housing were kept at 0.2 mm to ensure two-dimensional flow analysis.

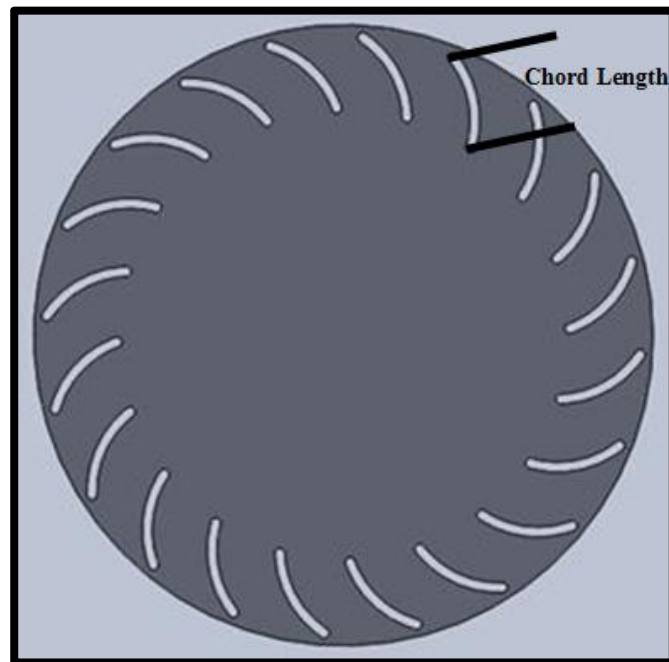


Figure 7. SolidWorks 20-bladed rotor model.

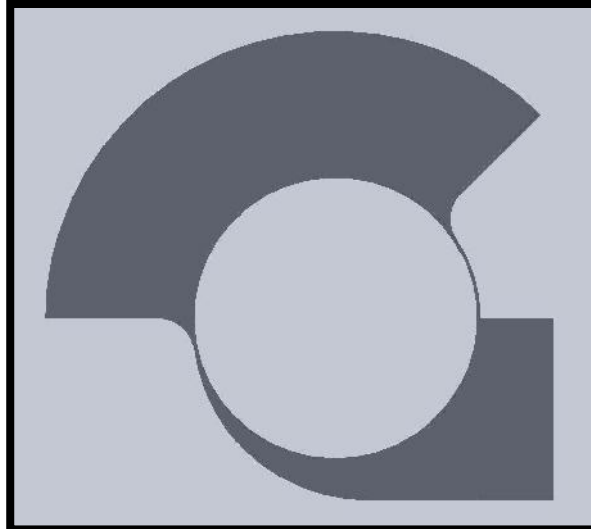


Figure 8. SolidWorks housing model. From [14].

Utilizing SolidWorks, a commercial solid modeling software application, a physical model of both the rotor and housing unit were constructed. These models were imported into ANSYS-CFX, a commercial CFD software package, for simulation and analysis. The simulations were conducted in two dimensions and were run in transient mode with the rotor rotating and the housing stationary. Upon successful mesh generation, the boundary conditions were established and initial conditions set. Using air as an ideal gas and an initial air velocity of 0 m/s, a series of simulations for the 20-bladed cross-flow fan were conducted at speeds from 4,000 to 10,000 rpm. Monitor points were created to monitor torque on the blades as well as mass flow at the inlet and outlet. These points allowed the user to determine when the simulation reached a stable transient state. As such, each simulation was conducted until the value of thrust was constant and the difference in mass flow rate between inlet and outlet converged to zero. This steady-state data was then measured and analyzed.

B. SIMULATION OVERVIEW

1. Rendering

The first step in conducting a flow analysis in ANSYS-CFX was to accurately import all components of the assembly into the program. Both the rotor and the housing were imported as separate components with an interface between the rotor and the

housing domains. This allowed the establishment of the housing as a stationary component while allowing the rotor to rotate freely at the desired speed. The components were labeled as named sections in Figure 9.

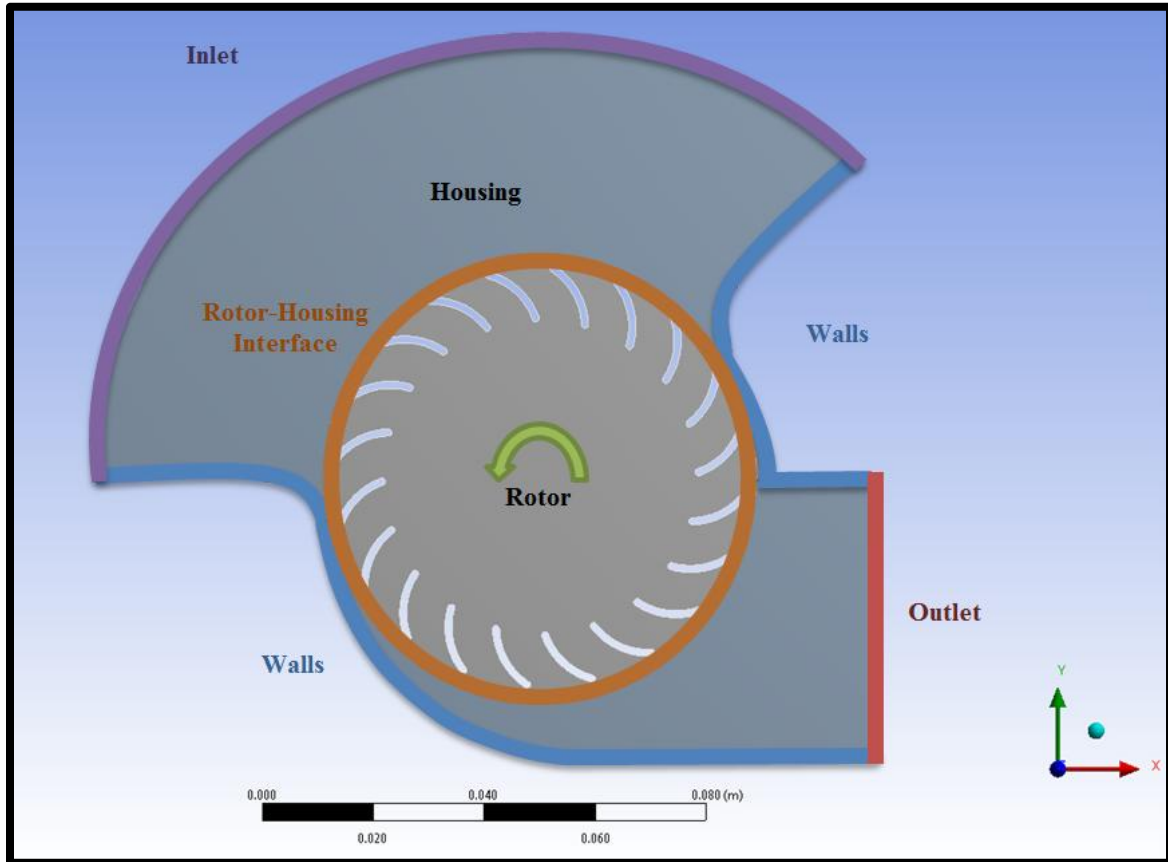


Figure 9. Named sections of rotor and housing.

2. Mesh Generation

Upon importing the rotor and housing into ANSYS-CFX, the model surfaces were labeled and an initial coarse mesh generated. After successfully modeling a coarse mesh, the mesh was refined to have sufficient resolution and maximum accuracy of the flow analysis during the simulation. By applying a sweep method and two levels of edge sizing, the resultant mesh in Figure 10 reached 850,732 nodes with 418,522 elements with a single element thickness.

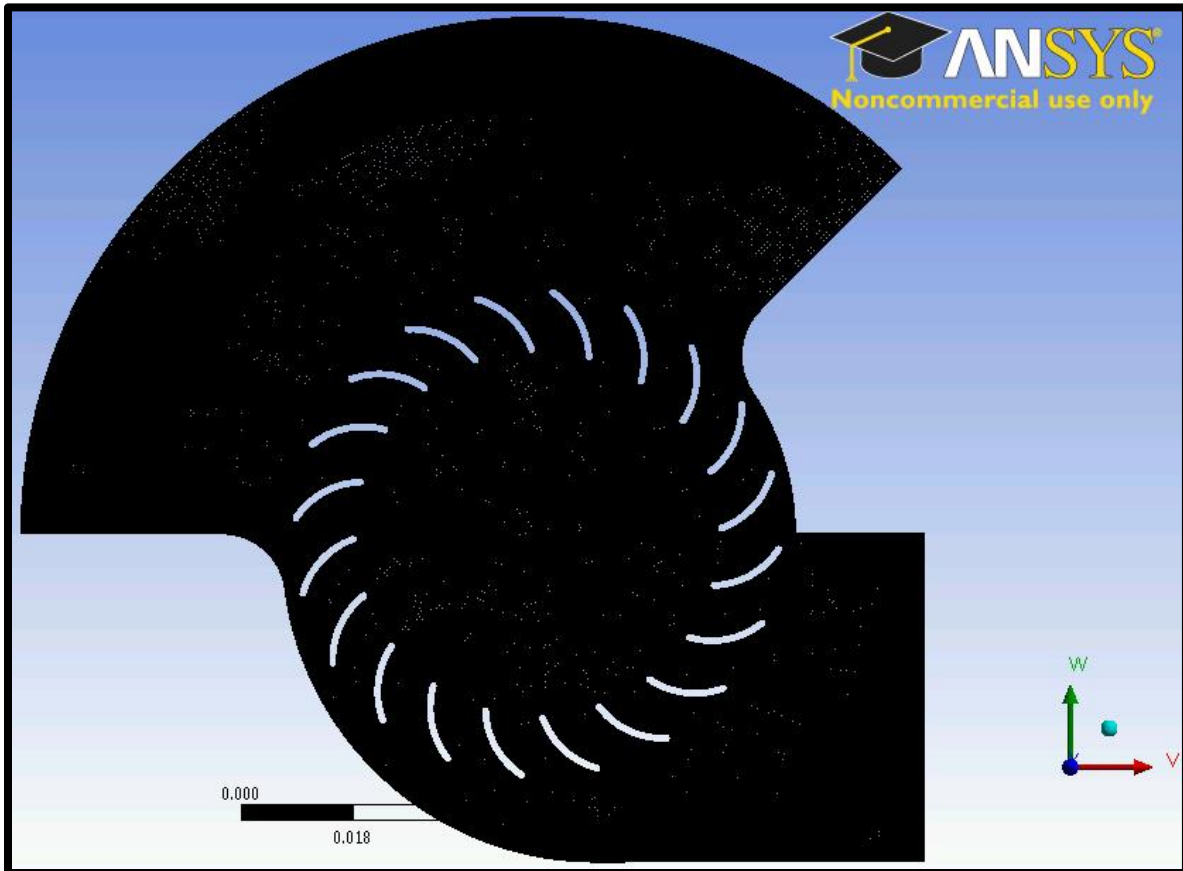


Figure 10. Two-dimensional mesh with 850,732 nodes.

One of the most important aspects of mesh generation was ensuring that the mesh sizes were similar at the rotor-housing interface. This increased the accuracy of the prediction as the fluid crossed the domain boundaries. The single element, which can be seen in Figure 11, allowed for more accurate two-dimensional analysis.

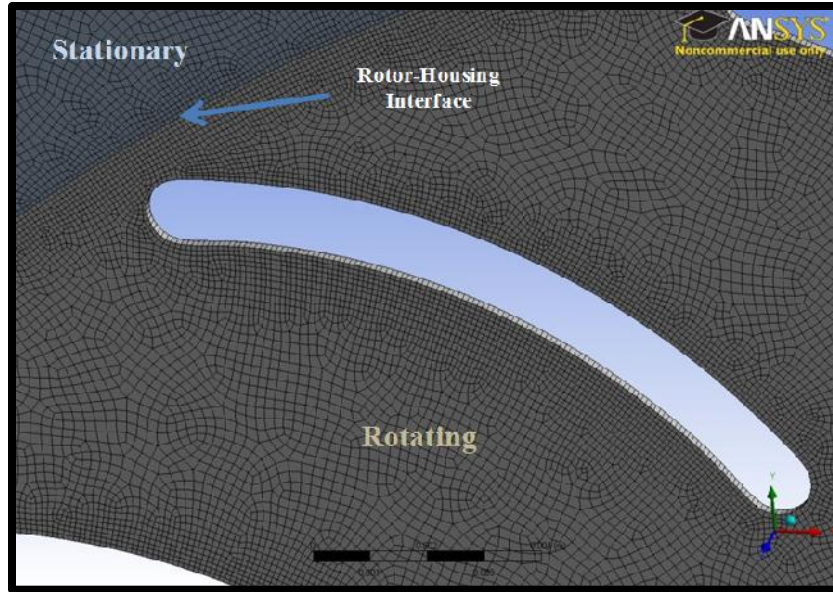


Figure 11. Close-up of rotor blade mesh with a single element thickness.

3. Setup

The analysis conducted was transient and the time-steps were calculated so that 1 degree of rotation of the rotor would coincide with a single time-step. As the 16-bladed rotor reached steady-state at approximately 5 revolutions, the total simulation time was adjusted to ensure that 6 revolutions would be conducted for each simulation. This allowed for a margin of error in the case that the 20-bladed rotor required an additional revolution to reach steady-state. The fluid simulated was air as an ideal gas at a relative pressure of 1 atmosphere, a temperature of 288.15 K, with an inlet turbulence intensity factor of 5 percent. To account for energy input into the model and turbulence in the air-flow, the total energy model and the k-epsilon turbulence models were used, respectively.

The named sections previously established were imported into CFX-Pre to define the suitable boundary conditions. The housing walls in the figure were considered no-slip walls as part of the rotor and housing default domains for the simulation. Due to the uncertainty of the flow at the beginning of the simulation, the housing inlet was modeled as an opening with 0 Pa stagnation pressure, while the outlet was modeled as an opening with 0 Pa average static pressure. Finally, the housing and rotor faces were modeled as

symmetry planes. The settings for 9,000 rpm can be found in Appendix A. The only variations in settings for various speeds were the difference in time-steps and total time. The values for each can be seen in Table 1.

Table 1. ANSYS-CFX settings for various speeds.

SPEED		TIME STEP	TOTAL TIME
[rpm]	[Rad/s]	[s]	[s]
4,000	418.879	4.17E-05	0.09
6,000	628.319	2.78E-05	0.06
8,000	837.758	2.08E-05	0.045
9,000	942.478	1.85E-05	0.04
9,500	994.838	1.75E-05	0.0379
10,000	1,047.198	1.67E-05	0.036

4. ANSYS-CFX CFD Analysis

The following equations are used by ANSYS-CFX for CFD analysis:

Continuity equation:
$$\frac{\partial \dots}{\partial t} + \nabla \cdot (\dots U) = 0$$

Momentum equation:
$$\frac{\partial \dots U}{\partial t} + \nabla \cdot (\dots U \otimes U) = \nabla \cdot \left(-p\mathbf{u} + \sim \left(\nabla U + (\nabla U)^T \right) \right)$$

Energy equation:
$$\frac{\partial \dots h_{tot}}{\partial t} - \frac{\partial \dots}{\partial t} + \nabla \cdot (\dots U h_{tot}) = \nabla \cdot (-\nabla T) + \nabla \cdot \left(-\nabla U + \nabla U^T - \frac{2}{3} \nabla \cdot U \mathbf{u} U \right)$$

$$h_{tot}(p, T) = h_{stat}(p, T) + \frac{1}{2} U^2$$

Turbulent eddy viscosity:
$$\sim_t = C_{\sim} \dots \frac{k^2}{\nu}$$

Turbulent kinetic energy:
$$\frac{\partial (\dots k)}{\partial t} + \nabla \cdot (\dots U k) = \nabla \cdot \left[\left(\sim + \frac{\sim_t}{\dagger_{\sim}} \right) \nabla k \right] + P_k - \dots \nu$$

Turbulent eddy dissipation:
$$\frac{\partial (\dots \nu)}{\partial t} + \nabla \cdot (\dots U \nu) = \nabla \cdot \left[\left(\sim + \frac{\sim_t}{\dagger_{\sim}} \right) \nabla \nu \right] + \frac{\nu}{\dagger_{\nu}} (C_{\nu 1} P_{\sim} - C_{\nu 2} \dots \nu)$$

The equation of state:
$$\dots(p, T) = \frac{p}{R_0 T}$$

Deformation rate tensor:
$$e_{ij} = \frac{dU_i}{dx_j}$$

Production term:
$$P_k = \sim_t e_{ij} e_{ij}$$

Where $C_{\sim} = 0.09$, $C_{\nu 1} = 1.44$, $C_{\nu 2} = 1.92$, $\dagger_{\sim} = 1.00$ and $\dagger_{\nu} = 1.30$

THIS PAGE INTENTIONALLY LEFT BLANK

III. EXPERIMENTAL SETUP

A. SOLIDWORKS DESIGN

In the wake of successful simulation and the determination of a promising thrust generation, a 78 mm, 20-bladed rotor and housing were designed and fabricated for experimentation and validation. Delagrange's [14] optimized housing design was utilized with a slight modification to the end-plates to decrease the assembly weight, as seen in Figure 12.

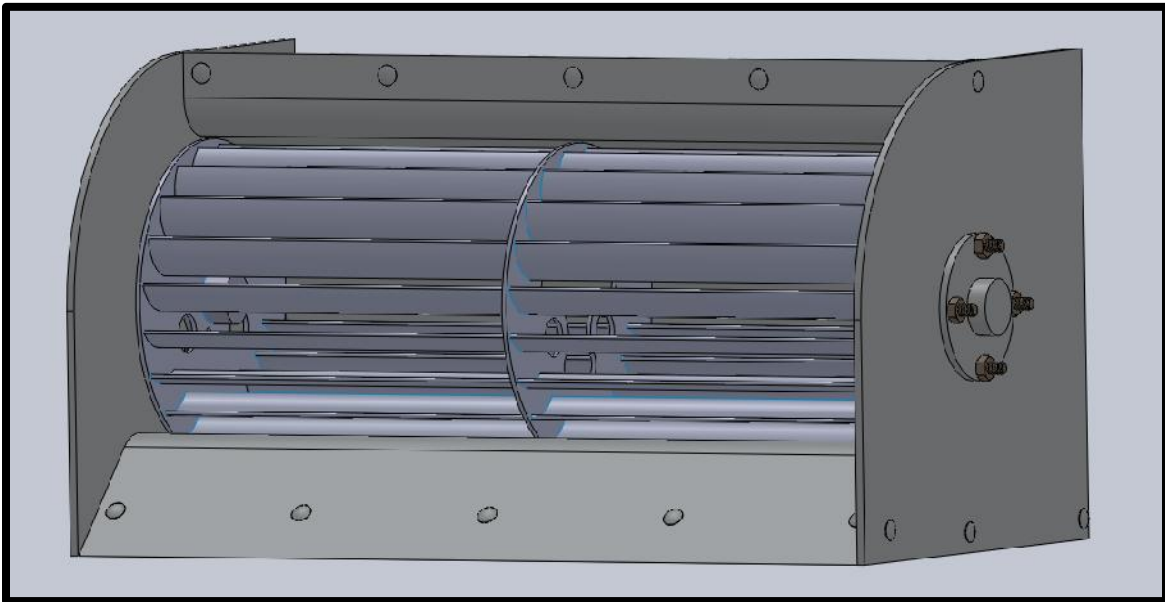


Figure 12. SolidWorks 20-bladed cross-flow fan assembly.

B. FABRICATION

1. Material Selection

To ensure the highest thrust-to-weight ratio, the housing and rotor were built of the strongest, most durable, and lightweight material feasible given the build constraints of the Turbopropulsion Laboratory. Carbon-fiber was the best possible candidate. As such, a 78 mm diameter and 210 mm span, 20-bladed carbon-fiber rotor was fabricated.

2. Design and Construction

The housing end-plates and the rotor support disk were cut utilizing pre-existing 1.5 mm thick carbon-fiber sheets. The rotor blades were made of carbon fiber reinforced composite tube with an inside diameter of 19.05 mm and an outer diameter of 20.96 mm. The tubes were cut lengthwise to produce curved airfoils of 11.08 mm chord length. Circular leading and trailing edges were used on the airfoils. The rotor was assembled with Loctite Hysol E-120HP epoxy and consisted of 20 blades, 2 end-plates, and a rigid support disk in the center to prevent flexing of the blades. This ensured a rigid rotor and more reliable flow throughout the cross-flow fan. Upper and lower portions of the housing molds are seen in Figure 13 and Figure 14, respectively. These models were used to cut the profile pieces from marine-grade plywood, which would be assembled into the wooden molds for manufacture of the custom carbon-fiber housing.

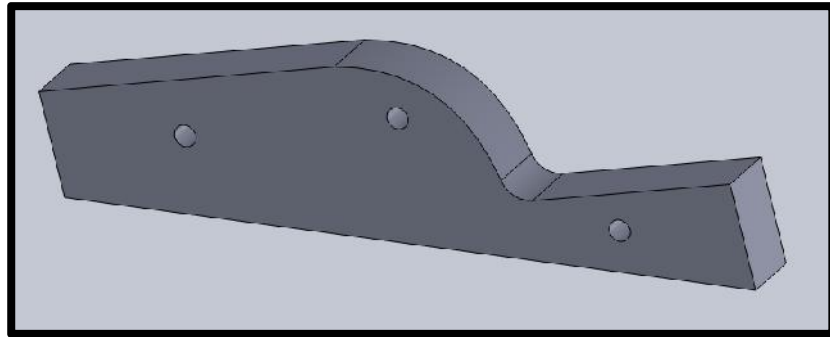


Figure 13. SolidWorks model for upper portion of housing mold.

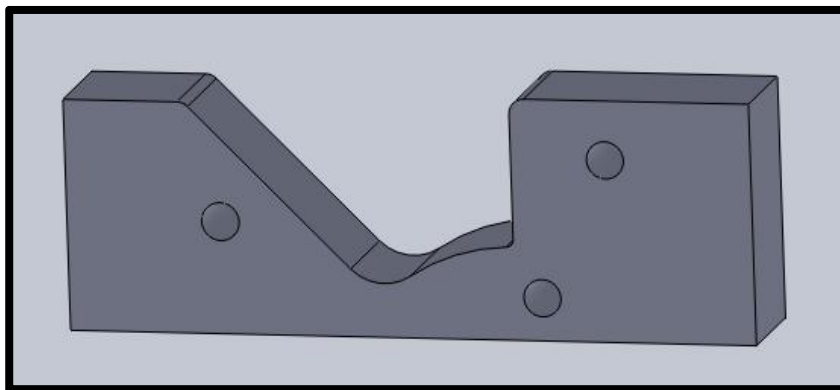


Figure 14. SolidWorks model for lower portion of housing mold.

The marine-grade plywood was assembled with epoxy to create the molds in Figure 15. Then, pre-preg carbon-fiber was vacuum-applied and heat-treated to create the housing components. Stiffeners were added to reduce the flexing of the housing.

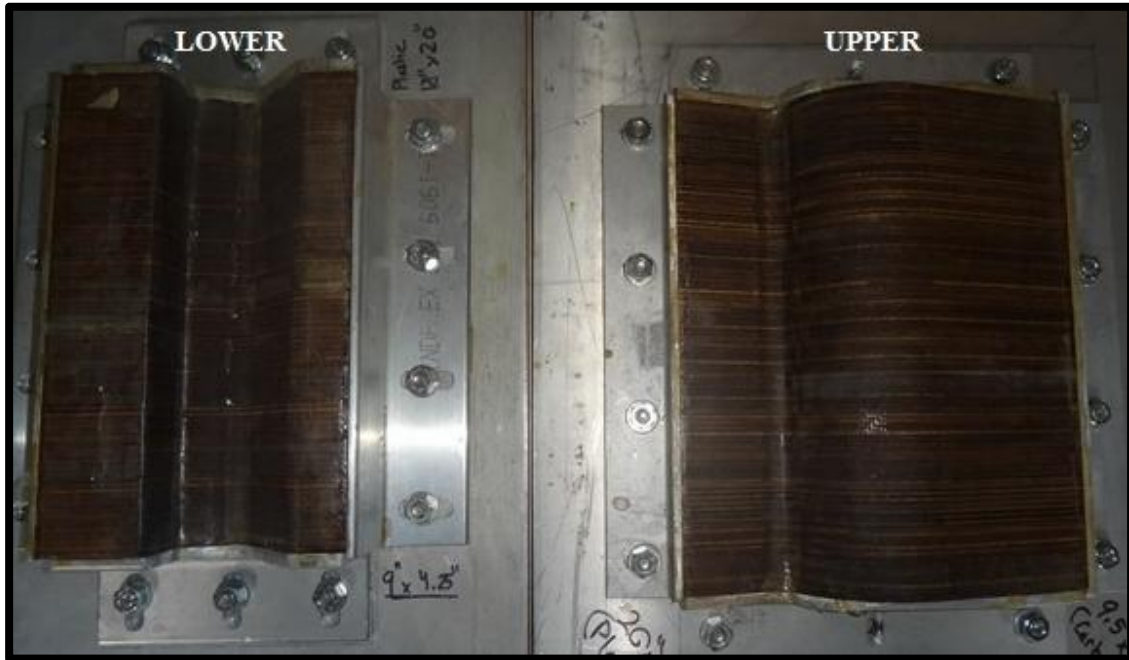


Figure 15. Custom wood carbon-fiber molds for the cross-flow fan housing.

3. Motor Selection

One of the most important aspects of the design was selecting a lightweight motor that would generate the highest speed and thrust with the lowest weight and power consumption possible. After a significant amount of research, Scorpion Motors 4025, 4035, and 5035 were selected for experimentation. The company specializes in model aircraft motors, which were optimum for the application due to their relatively low weight and ability to produce high speeds, as seen in Appendix B. The selected motors are pictured in Figure 16.



Figure 16. Scorpion Motors 4025, 4035, and 5035, respectively. From [17].

Another important aspect of designing a cross-flow-fan propulsion system was selecting a suitable battery to power the motors. The ideal battery would supply a sufficient amount of power to the motor without adding too much weight. As such, the assembly required a battery with extremely high power density. Scorpion motors recommended the lithium polymer battery in Figure 17, which is rated at 5000mAh and 22.2V.



Figure 17. Thunder Power RC lithium polymer battery.

C. EQUIPMENT SETUP

1. Cross-flow Fan Assembly

The cross-flow fan assembly consisted of the carbon-fiber rotor, housing, and motor. A bearing and housing was mounted on one end-plate and the motor was mounted on the opposite end-plate. The motor was connected to one end of the rotor by a 5.98 mm shaft that was locked into the rotor bushing with a set screw. The entire unit was assembled with fasteners that allowed for quick and easy removal and replacement of the rotor, housing, and motor.

2. Test Platform

The test platform for the cross-flow fan assembly can be seen in Figure 18. It consisted of a sliding bracket upon which the cross-flow-fan assembly was mounted. A triple-beam balance (Figure 19) or digital scale (Figure 20) with remote read out was placed below with a 0.6096 m by 0.3048 m aluminum plate from which thrust could be measured. The cross-flow fan was oriented so thrust could be easily measured by the balances. The modular design allowed for multiple cross-flow fan configurations and provided a versatile testing environment.

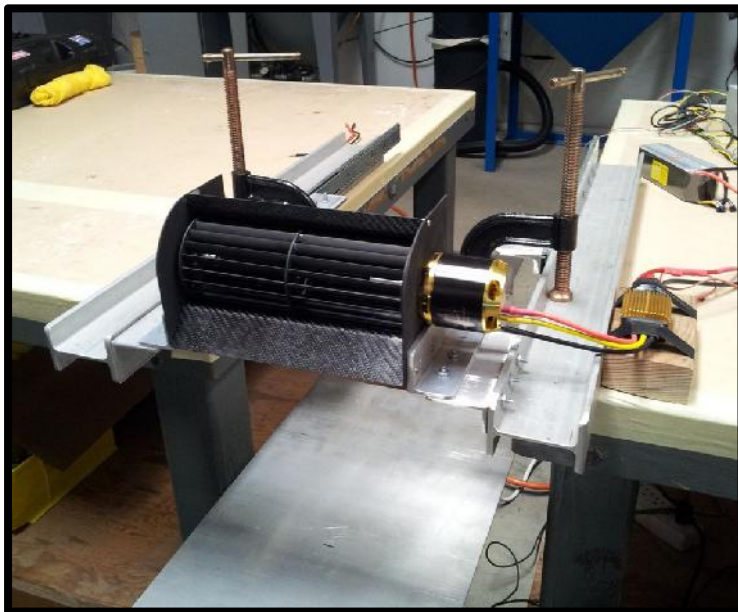


Figure 18. Test platform and cross-flow fan assembly.

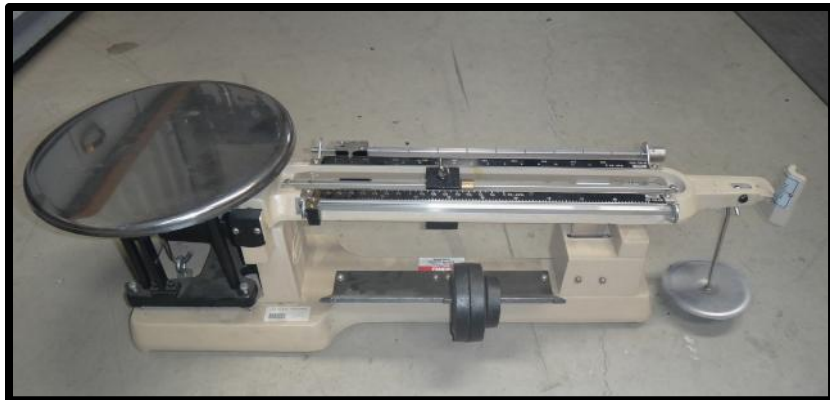


Figure 19. Triple-beam balance used for measuring thrust.



Figure 20. Digital balance used for thrust measurement.

3. Cross-flow Fan Control

The next step was to select a control method for the motor. The Scorpion motor could be controlled remotely, digitally, or with a potentiometer. Each method controls the speed of the motor by varying the amount of voltage supplied from the battery in the form of pulses. As the frequency of the pulsed voltage was increased, the motor speed increased. Initial testing proved the potentiometer shown in Figure 21 to be the most effective.

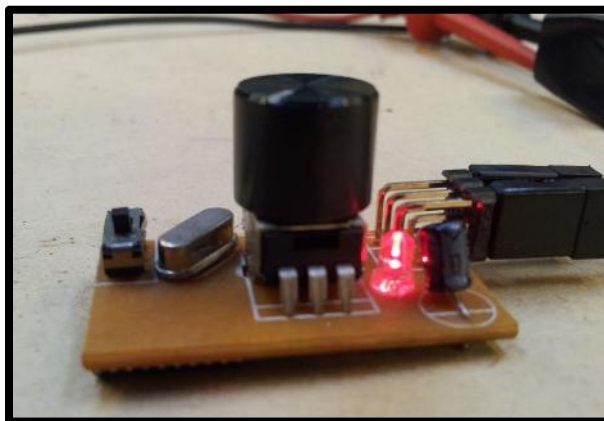


Figure 21. Scorpion motor potentiometer.

The potentiometer was modified into the user-friendly control unit in Figure 22 and integrated into the system. Because the batteries would drain quickly at high speeds, the strobe tachometer in Figure 23 was used to verify rotor speed prior to taking speed measurements.

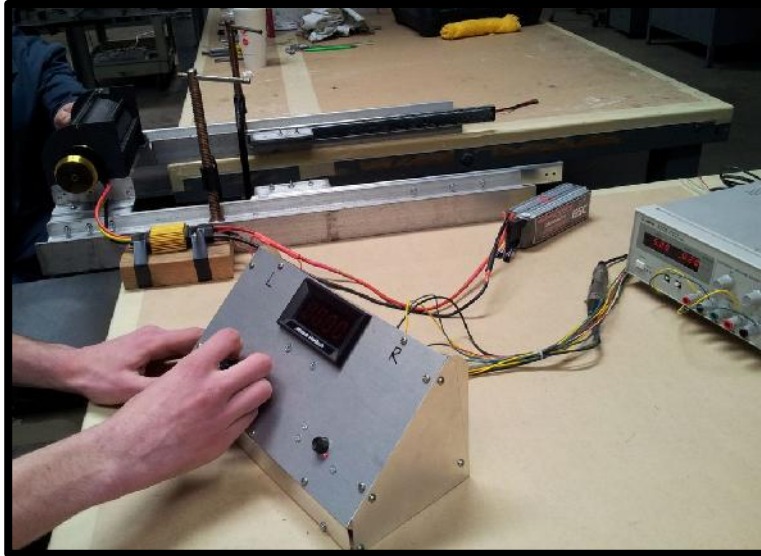


Figure 22. Potentiometer motor control assembly.



Figure 23. Strobe tachometer used to measure speed.

4. Instrumentation

Voltage and current measurements were taken at each speed to determine values of power. The voltage was measured with the Fluke multimeter shown in Figure 24, and

the clip-on ammeter in Figure 25 was used to measure current. Speed was verified with a strobe tachometer and thrust was measured using a triple-beam balance.



Figure 24. Fluke multimeter used to measure voltage.



Figure 25. Clip on ammeter used to measure current.

5. Data Acquisition

Each run was conducted with the highest speed first and then successively lower speeds due to the power requirements on the battery. An initial battery voltage was taken. Then the triple-beam balance was set to the approximate thrust value for ease of measurement and the strobe tachometer was set to the desired speed. The run was started by turning the potentiometer to the desired speed and fine-tuning it to match the speed set by the tachometer. Once the desired speed was reached, the current and thrust values were recorded and the potentiometer dialed back down to zero. A final battery voltage was taken when the run was complete.

One issue encountered during the data acquisition phase was the accuracy of the current measurement. The Scorpion motor's speed is controlled by varying the amount of current supplied to the battery, in the form of short bursts, also known as pulsed DC current. This pulsed DC current is difficult to accurately measure and the clip-on

ammeter's reading could be incorrect. In an effort to validate the experimental results, an additional set of experiments was conducted utilizing a similar setup to that of Delagrangé [14]. For this series of runs, a router was used in place of the motor to drive the rotor and the router was plugged into a 120V 60HZ VARIAC vice using the battery and potentiometer. The VARIAC allowed for the variation of the applied voltage to the router, which varied its speed. This setup can be seen in Figure 26.

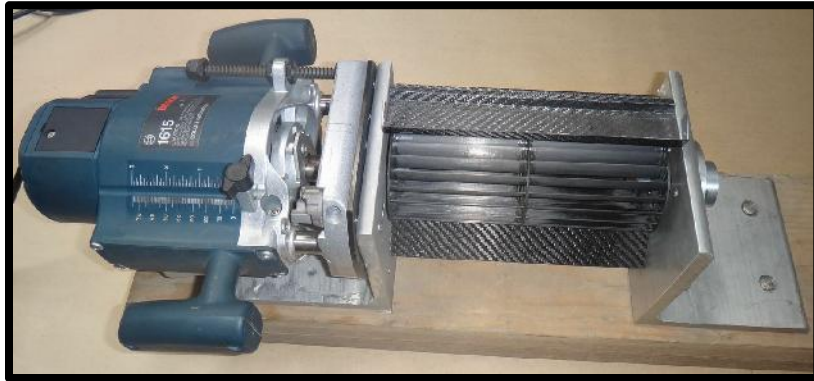


Figure 26. Experimental setup with router.

THIS PAGE INTENTIONALLY LEFT BLANK

IV. RESULTS AND DISCUSSION

A. DATA CONVERGENCE

Delagrange [14] and Yu [16] observed that steady-state values for their respective simulations were reached after 5 revolutions of the cross-flow fan. Because the steady-state was not previously identified for the 20-bladed rotor, the simulations were conducted with 6 full revolutions. Verification of steady-state was conducted by observing the difference in mass flow at the inlet and outlet, and ensuring conservation of mass. The mass-flow convergence for the 9,000 rpm simulation is depicted in Figure 27. At 6 revolutions, the delta mass flow reached a value of $1.0e^{-7}$ kg/s.

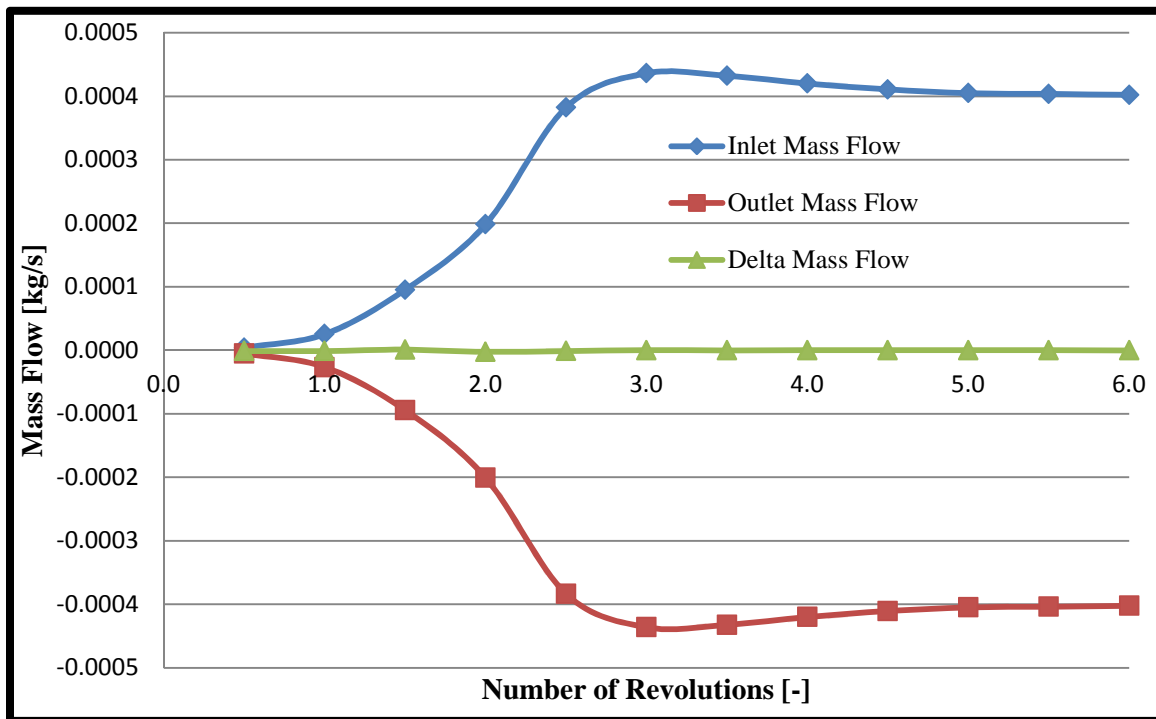


Figure 27. Conservation of mass verification at 9,000 rpm.

The torque converged to a value of $9.157e^{-4}$ Nm after six revolutions as in Figure 28. A complete set of the analytical data is tabulated in Appendix C.

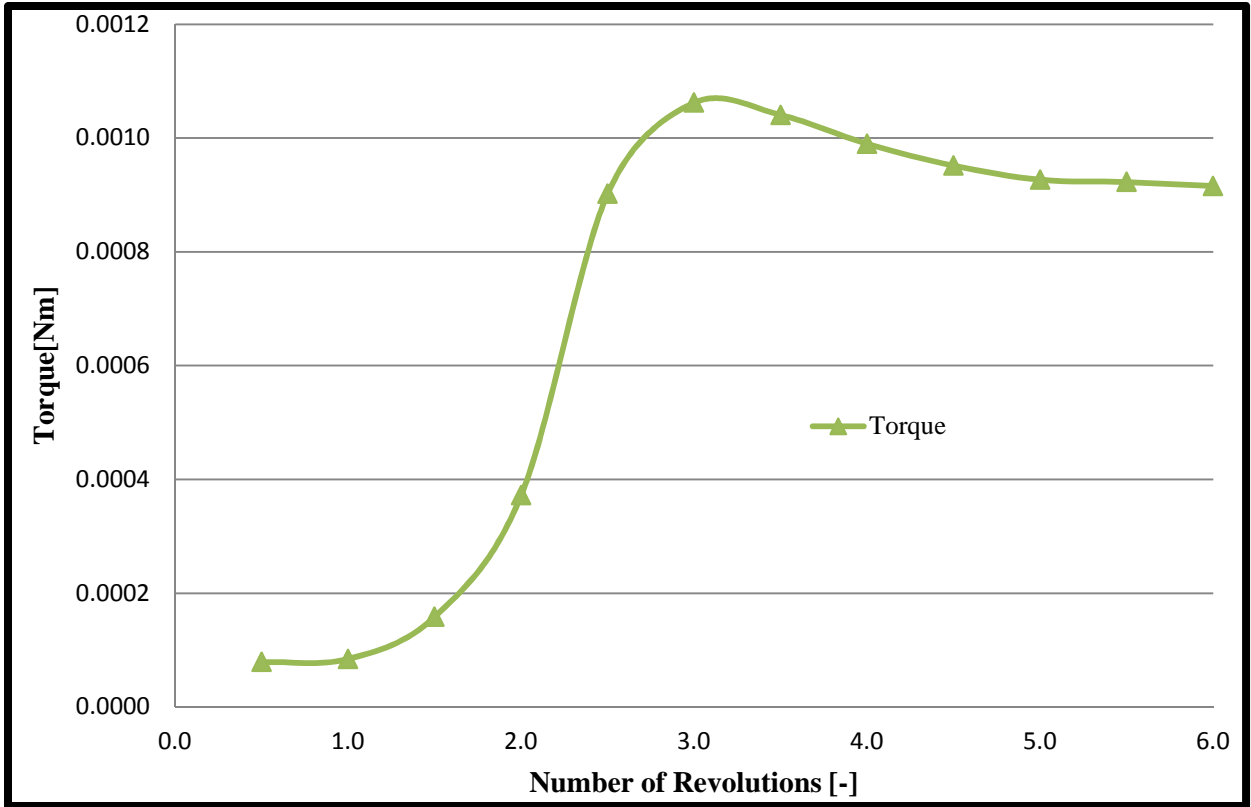


Figure 28. Torque convergence at 9,000 rpm.

B. FLOW VISUALIZATION

Two sets of simulations were conducted to compare k-epsilon and laminar flow modeling. It is evident from the k-epsilon flow visualization in Figure 29 that a large counter-clockwise vortex forms on the inner right side of the 20-bladed rotor. The laminar model flow visualization in Figure 30 had an additional counter-clockwise vortex near the top of the rotor. Both models demonstrated very little rotor-blade-tip leakage at the inlet, however, there was apparent leakage near the housing walls on the right side of the rotor. This was consistent with the findings of Delagrange [14] and his 16-bladed rotor at 8,000 rpm.

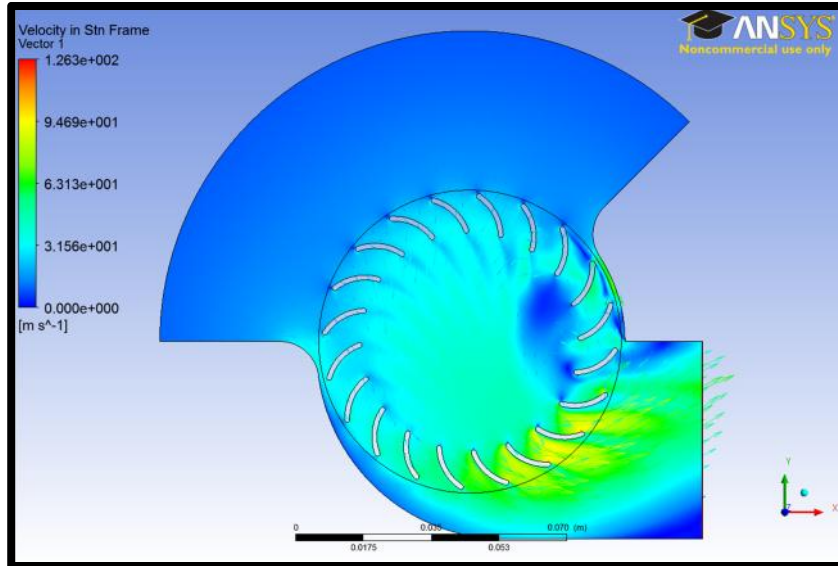


Figure 29. K-epsilon turbulence model flow visualization at 9,000 rpm.

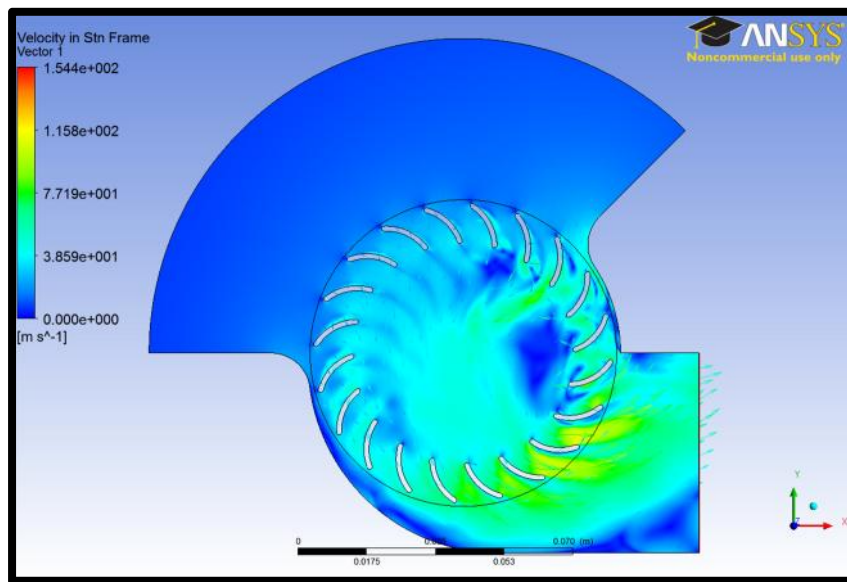


Figure 30. Laminar flow model visualization at 9,000 rpm.

Closer investigation of both models revealed an additional clockwise vortex forming close to the right side wall of the cross-flow fan. This vortex in Figure 31 allowed fluid to flow in the opposite direction of the rotor on the outer side of the blades.

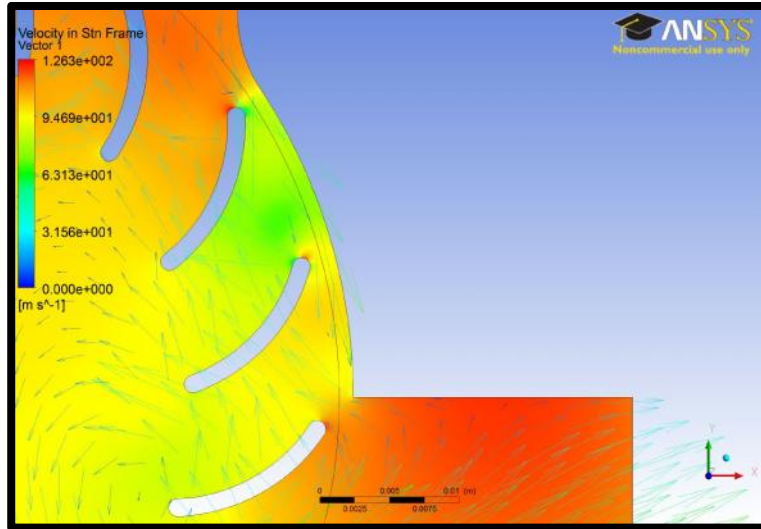


Figure 31. Close-up of k-epsilon flow field at 9,000 rpm showing vectors and vortices.

Also evident in Figure 32 is a small amount of recirculation flow back into the lower edge of the outlet. This was consistent with both models. With the exception of velocity, only minor variations were present in the flow fields at each speed, which can be seen in Appendix D.

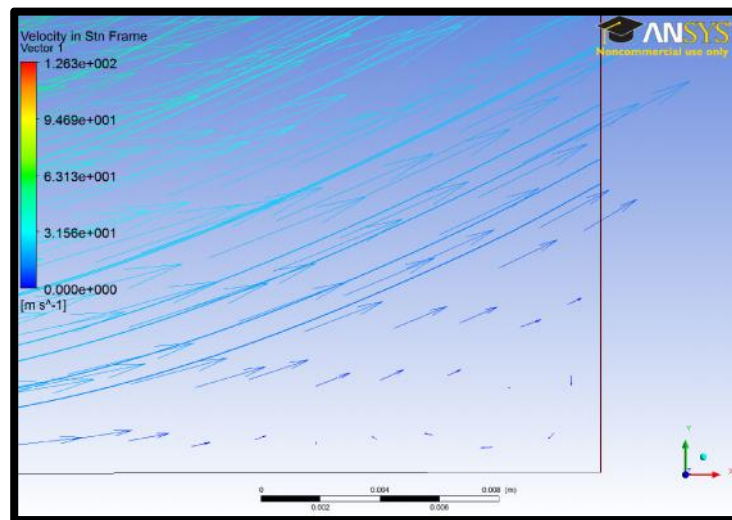


Figure 32. Close-up of k-epsilon recirculation flow in outlet at 9,000 rpm.

Figure 33 and Figure 34 shows the velocity streamlines and resultant vectors developed in the cross-flow fan at 9,000 rpm for both the k-epsilon and laminar flow

models, respectively. Of note is the fact that no stalled blades exist along the entire inlet or outlet. Stall only occurred along the housing walls, which was expected as it is consistent with [14]. One major difference between the two flow models was that the back-flow present in the laminar flow model is much more pronounced than its k-epsilon counterpart. Additionally, it was evident that the fluid exits the cross-flow fan at a substantial angle. Using the function calculator for the k-epsilon model, the u and v components of velocity were determined to be 42.28 m/s and 20.91 m/s, respectively. These values were used in the equation below to determine the average flow angle at the outlet to be 26.32 degrees for 9,000 rpm. The streamlines at all speeds were all very similar and can be seen in Appendix E.

$$\theta = \tan^{-1}\left(\frac{u}{v}\right)$$

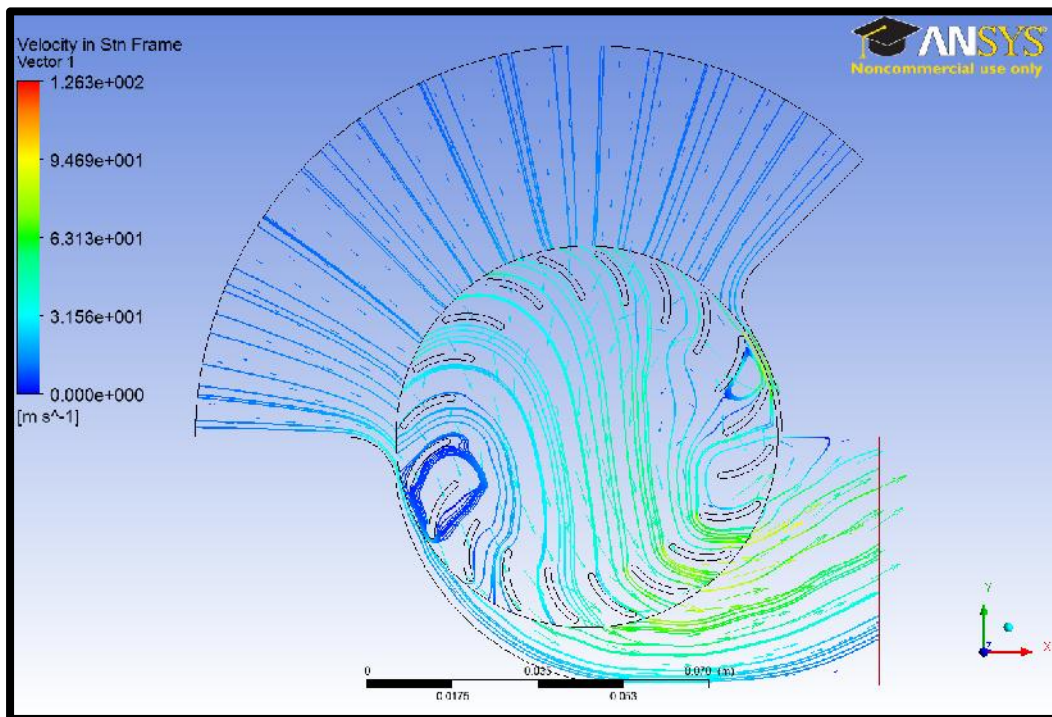


Figure 33. Streamlines at 9,000 rpm with the k-epsilon turbulence model.

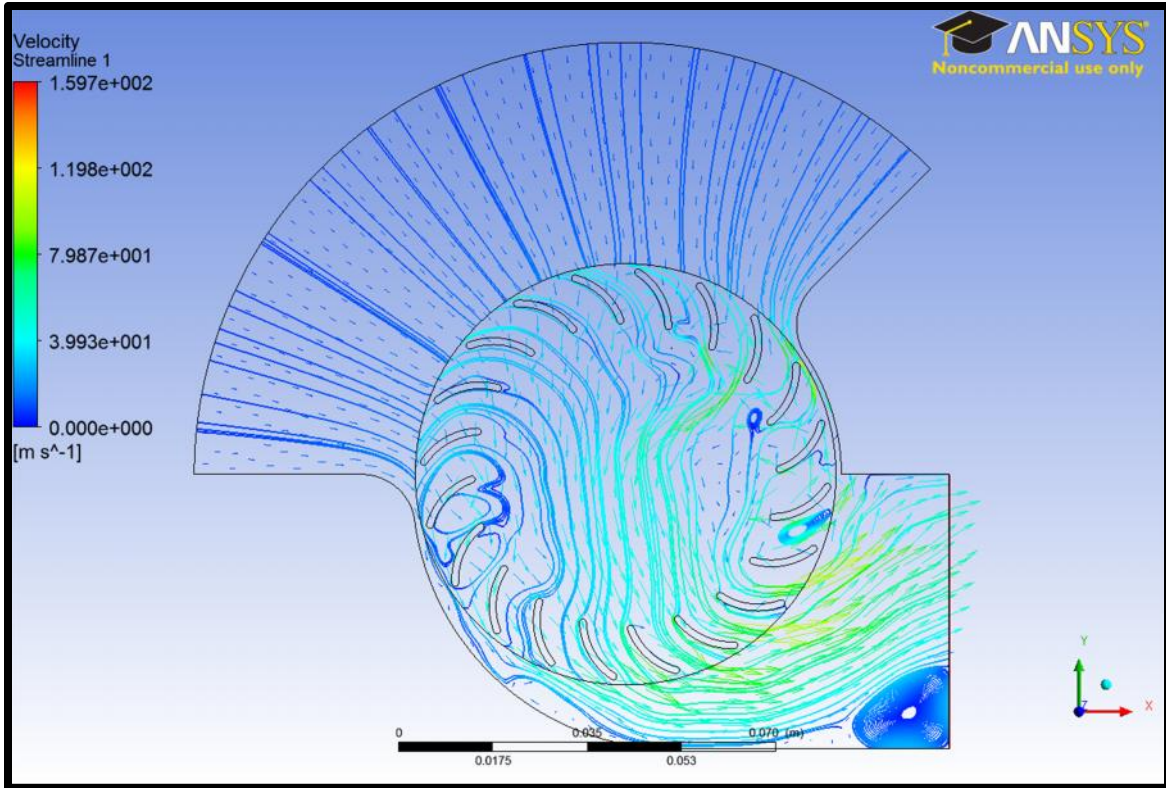


Figure 34. Laminar flow model streamlines at 9,000 rpm.

C. ANALYTICAL VERSUS EXPERIMENTAL RESULTS

1. Thrust

Thrust values were determined analytically from ANSYS-CFX for both the k-epsilon turbulence model and the no turbulence laminar model. Thrust values were determined experimentally with both the router and the Scorpion 4025 motor setup. Both sets of experimental and analytical values of thrust are plotted in Figure 35. It is important to note that the assumption of unsteady laminar flow did not result in an appreciable change in analytical thrust.

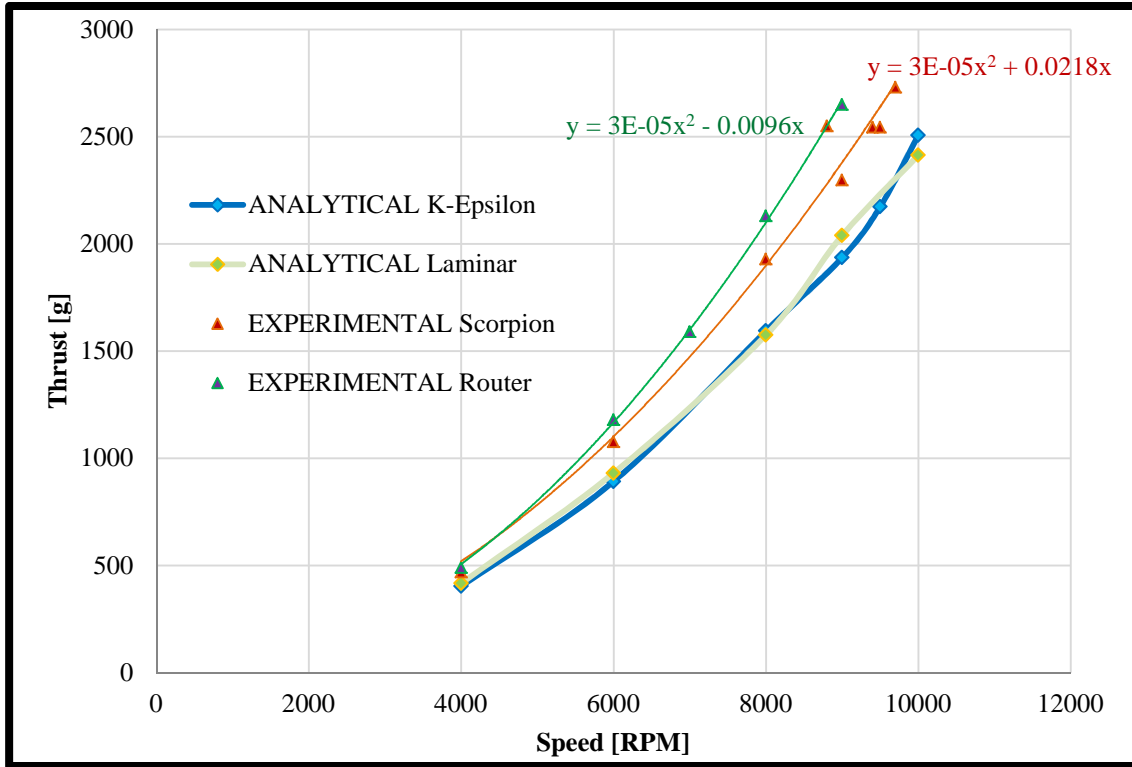


Figure 35. Analytical and experimental thrust comparison.

Averaged values of thrust obtained experimentally can be seen in Table 2. The complete set of experimental test data is located in Appendix F.

Table 2. Experimental thrust values.

SPEED	SCORPION	ROUTER
[rpm]	THRUST [g]	THRUST [g]
0	0	0
4,000	469	490
6,000	1076	1180
7,000	-	1590
8,000	1,929	2130
9,000	2,298	2650
9,500	2,544	-
9,700	2,730	-

The function calculator in ANSYS-CFX was used to calculate the mass flow and velocity at the cross-flow-fan outlet for the 0.2 mm section. These values were then multiplied by 1,015 to account for the length of the rotor and used in the equations below

to arrive at the values of thrust in Table 3. The complete set of analytical data can be found in Appendix C.

$$Thrust[N] = \dot{m}_{outlet} U_{outlet}$$

$$Thrust[g] = \frac{Thrust[N]}{0.00981}$$

Table 3. Thrust values determined analytically via ANSYS-CFX.

K-EPSILON MODEL					
SPEED		VELOCITY	MASS FLOW	THRUST	
[rpm]	[Rad/s]	[m/s]	[kg/s]	[N]	[g]
4,000	418.879	20.922	0.194	3.958	403.612
6,000	628.319	31.573	0.284	8.748	892.056
8,000	837.758	42.549	0.376	15.633	1594.116
9,000	942.478	47.434	0.410	18.986	1936.069
9,500	994.838	50.410	0.433	21.314	2173.423
10,000	1047.198	53.731	0.469	24.586	2507.099
LAMINAR FLOW MODEL					
SPEED		VELOCITY	MASS FLOW	THRUST	
[rpm]	[Rad/s]	[m/s]	[kg/s]	[N]	[g]
4,000	418.879	23.141	0.177	4.087	416.776
6,000	628.319	36.139	0.253	9.129	930.896
8,000	837.758	46.234	0.334	15.450	1575.467
9,000	942.478	51.415	0.389	20.000	2039.429
10,000	1047.198	56.386	0.420	23.675	2414.223

2. Velocity Profiles

The velocity profiles in Figure 36 and Figure 37 were determined by inserting a line probe with 100 points from top to bottom along the outlet of the cross-flow fan in ANSYS-CFX. Similar to [14], it was evident that there is a large variation in the velocity values across the outlet boundary for both flow models. The outlet velocity ranges as low as 0 m/s and as high as 64 m/s in the k-epsilon model and from 1 m/s to 61 m/s in the laminar flow model. As previously noted, the cross-flow-fan outlet produced a stream of fluid at an approximate angle of 26.32 degrees. This angle resulted in the decreased velocity in the lower edge of the outlet. The decreased velocity in the upper portion of the outlet was due to the low pressure area and flow stagnation that occurs near the top wall of the outlet. It is also important to note that velocity decreases to zero near the lower

wall and the outlet. This is due to the recirculation flow that occurred in this region and the fact that ANSYS-CFX placed a wall at the outlet in the vicinity of the back-flow. This occurs in both flow models, however, the back-flow present in the laminar flow model is much greater than that of the k-epsilon model. This trend was consistent for velocity profiles at all speeds.

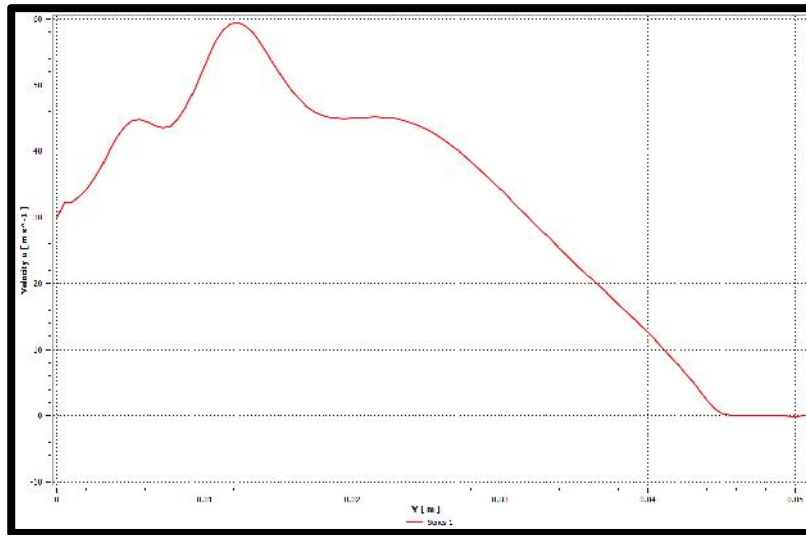


Figure 36. K-epsilon velocity profile at 9,000 rpm.

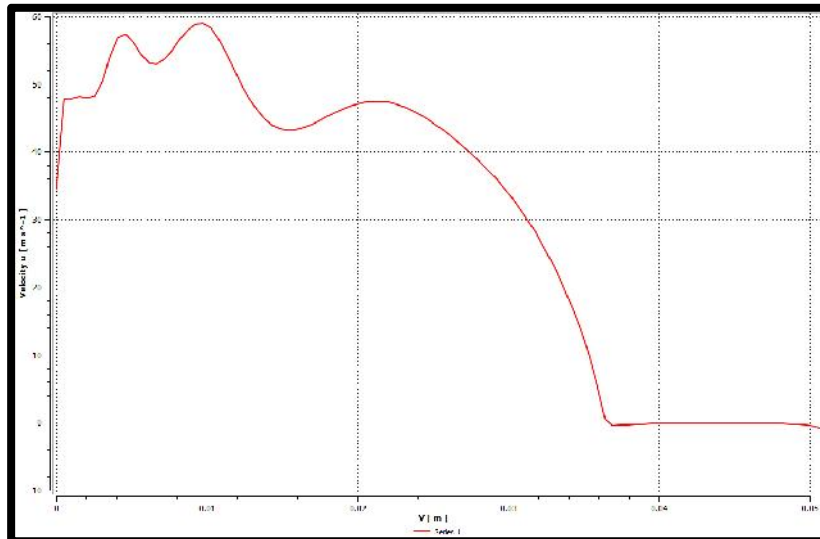


Figure 37. Laminar model velocity profile at 9,000 rpm.

3. Power

Experimental and analytical values of power are compared in Figure 38. It was noted that the experimental power was much higher than its analytical counterpart and that as the speed of the rotor increased, the disparity between the experimental and analytical power was even greater. This was likely due to the reduced efficiency at speeds higher than 6,000 rpm that was noted by Antoniadis [11] and Delagrange [14] during their research. The disparity encountered here, however was much greater than that of Delagrange [14]. In an effort to validate the experimental results, the router setup was utilized to conduct an additional series of tests. The results were very close to those found with the Scorpion motor setup. However, there was a slightly higher disparity in power when compared to the analytical model. With this outcome and the experimental results validated, it was necessary to revisit the turbulence modeling set in ANSYS-CFX. Previously, the analytical fluid model was set to k-epsilon for turbulence modeling. The flow may not have been best described with this model. The estimated maximum Reynold's number on the blades, based on chord, was in excess of 1 million. However, the flow was highly unsteady and reverses in direction relative to the blades during only half a revolution. Hence, the flow likely did not have enough time to become turbulent and it was deemed acceptable to analyze the boundary layer as laminar. At 9,000 rpm, there was a 38.8 percent increase in power, which was much closer to power values determined experimentally. Overall, the laminar flow model resulted in much more consistent values of power than the k-epsilon turbulence model.

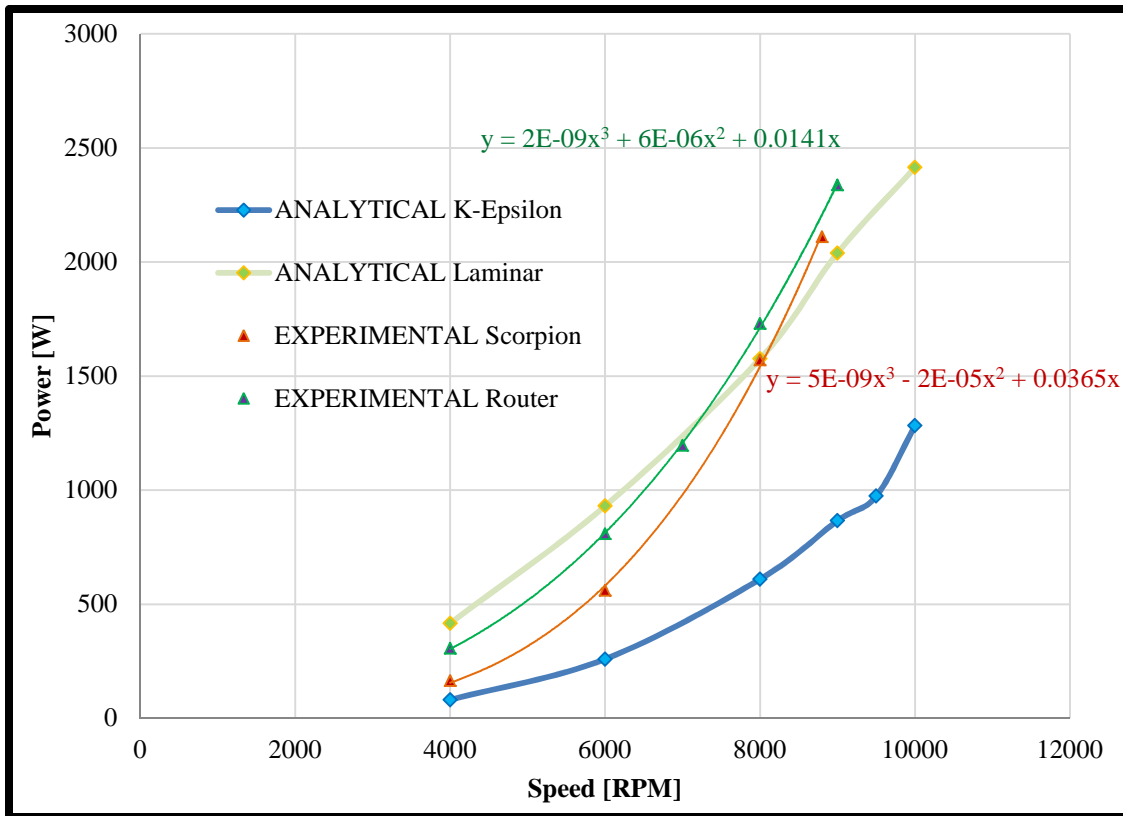


Figure 38. Analytical and experimental power comparison.

To determine power experimentally, voltage measurements were taken before and after each run while the current was measured during the run. The average of the initial and final voltages was calculated and these values were plugged into the power equation below to calculate electric power consumed during each run. Power values for the router setup were found by measuring the current and voltage during the run and then plugging them into the power equation below. The values for both sets of experiments are listed in Table 4.

$$V_{avg} = \frac{V_{initial} - V_{final}}{2}$$

$$P_{elec} = VI$$

Table 4. Experimental power.

LiPo BATTERY AND SCORPION 4025 MOTOR			
SPEED	CURRENT	VOLTAGE	POWER
[rpm]	[A]	[V]	[W]
4,000	7.10	23.32	165.57
6,000	23.90	23.45	560.46
8,000	65.90	23.82	1,569.74
8,800	88.60	23.82	2,110.45
ROUTER SETUP			
SPEED	CURRENT	VOLTAGE	POWER
[rpm]	[A]	[V]	[W]
4,000	7.5	41	307.5
6,000	13.27	61	809.47
7,000	16.62	72	1196.64
8,000	20.6	84	1730.4
8,800	24.1	97	2337.7

The function calculator in ANSYS-CFX was used to determine the torque on the rotor blades. The power was then calculated with the equation below and inserted into Table 5.

$$P = \tau \dot{\theta}$$

Table 5. Analytical Power

K-EPSILON TURBULENCE MODEL			
SPEED		TORQUE	POWER
[rpm]	[Rad/s]	[Nm]	[W]
4,000	418.879	0.194	81.471
6,000	628.319	0.414	259.824
8,000	837.758	0.728	610.038
9,000	942.478	0.919	866.285
9,500	994.838	0.979	973.813
10,000	1047.198	1.225	1282.714
LAMINAR FLOW MODEL			
SPEED		TORQUE	POWER
[rpm]	[Rad/s]	[Nm]	[W]
4,000	418.879	0.238	99.606
6,000	628.319	0.457	286.882
8,000	837.758	0.781	654.271
9,000	942.478	1.276	1203.001
9,500	994.838	1.276	1335.870
10,000	1047.198	1.276	1335.870

V. DESIGN, FABRICATION, AND TESTING OF FLYING PLATFORM

A. PLATFORM DESIGN

After determining a sufficient thrust and successfully validating analytical results experimentally, the time to design a platform capable of vertical take-off had come. The components were weighed individually and listed in Table 6.

Table 6. Weight of cross-flow-fan assembly with possible motors.

4025 SETUP		4035 SETUP		5035 SETUP	
COMPONENT	WEIGHT [g]	COMPONENT	WEIGHT [g]	COMPONENT	WEIGHT [g]
3" 20B ROTOR	105	3" 20B ROTOR	105	3" 20B ROTOR	105
CFF HOUSING	124	CFF HOUSING	124	CFF HOUSING	124
4025 MOTOR	357	4035 MOTOR	464	5035 MOTOR	693
MOTOR CONTROLLER	195	MOTOR CONTROLLER	195	MOTOR CONTROLLER	195
BATTERY	813	BATTERY	813	BATTERY	813
CONNECTORS	25	CONNECTORS	25	CONNECTORS	25
IR RECEIVER	6	IR RECEIVER	6	IR RECEIVER	6
TOTAL WEIGHT	1,625	TOTAL WEIGHT	1,732	TOTAL WEIGHT	1,961

The thrust-to-weight ratios were then calculated via the equation below and listed in Table 7 for comparison at the speeds obtained by each motor. It was evident that the optimum selection for motor was the 4025. This motor achieved higher thrust-to-weight ratios at lower speeds, which is more sustainable than its counterparts.

$$Ratio = \frac{Thrust[g]}{Weight[g]}$$

Table 7. Thrust-to-weight ratios for each motor.

SPEED	4025 MOTOR		4035 MOTOR		5035 MOTOR	
	THRUST	RATIO	THRUST	RATIO	THRUST	RATIO
[rpm]	[g]	[-]	[g]	[-]	[g]	[-]
4,000	469	0.28841	[-]	[-]	[-]	[-]
6,000	1,076	0.66236	[-]	[-]	[-]	[-]
7,000	1,929	1.18687	1369	0.79042	[-]	[-]
8,000	1,800	1.10769	1800	1.03926	[-]	[-]
8,500	2,000	1.23077	[-]	[-]	2050	1.04539
8,700	2,200	1.35385	[-]	[-]	[-]	[-]
8,800	2,550	1.56923	[-]	[-]	[-]	[-]
9,000	2,295	1.41231	2,300	1.32794	[-]	[-]
9,400	[-]	[-]	2,544	1.46882	[-]	[-]
9,500	[-]	[-]	2,544	1.46882	[-]	[-]
9,700	[-]	[-]	2,730	1.57621	[-]	[-]

After selecting a motor, it was necessary to design a platform upon which all components could successfully be mounted without adding too much weight. The platform had to be lightweight and easy to fabricate without sacrificing the thrust-to-weight ratio. As such, a configuration with two motors and four fans was decided upon and designed in SolidWorks as seen in Figure 39.

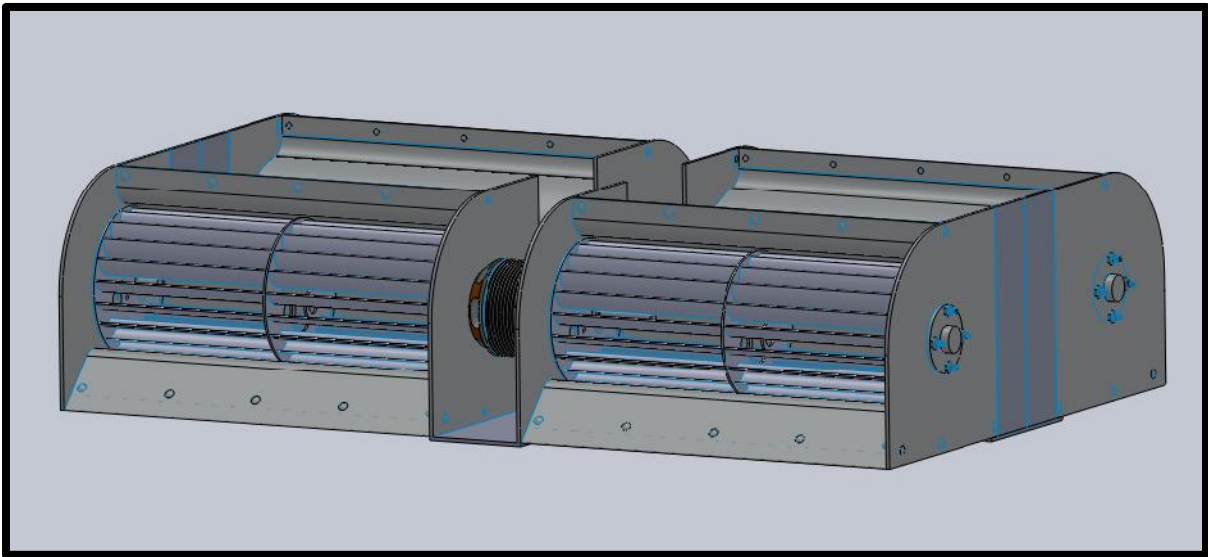


Figure 39. SolidWorks platform design.

B. PLATFORM FABRICATION

Due to the simplicity of the mounting platform, a carbon-fiber mold was built of aluminum, as in Figure 40. Pre-preg carbon-fiber was then cut, layered-up, and vacuum heat-treated to create the platform chassis.

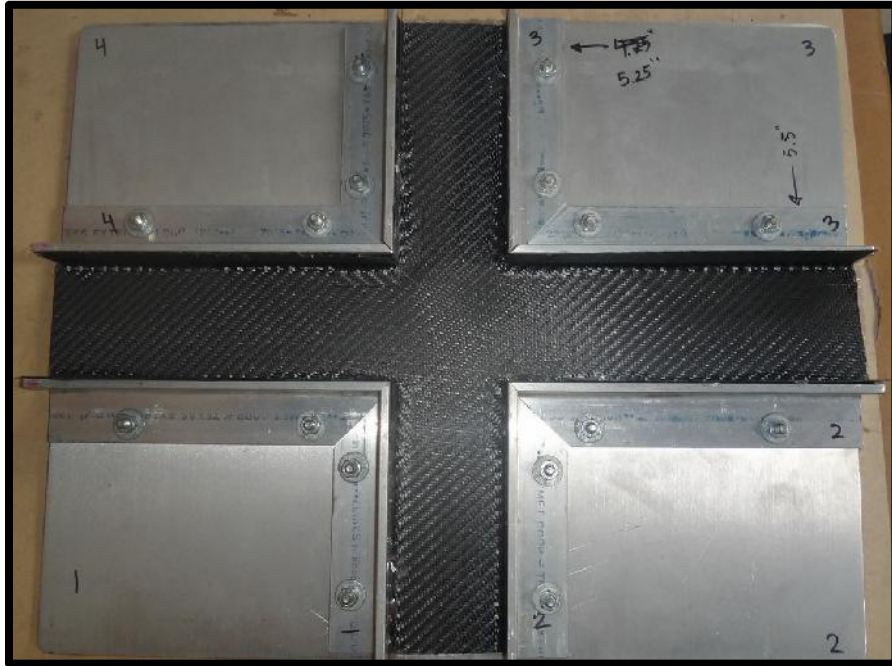


Figure 40. Aluminum carbon-fiber mold for test platform.

Four additional carbon-fiber rotors and cross-flow-fan housings were fabricated and assembled. For structural stability, the endplates were modified to encompass the two cross-flow fans. The test platform in Figure 41 was then assembled onto the mounting platform, adding stiffeners as necessary and legs to raise the platform off the ground. The resulting test platform weight was 4.14 kg.

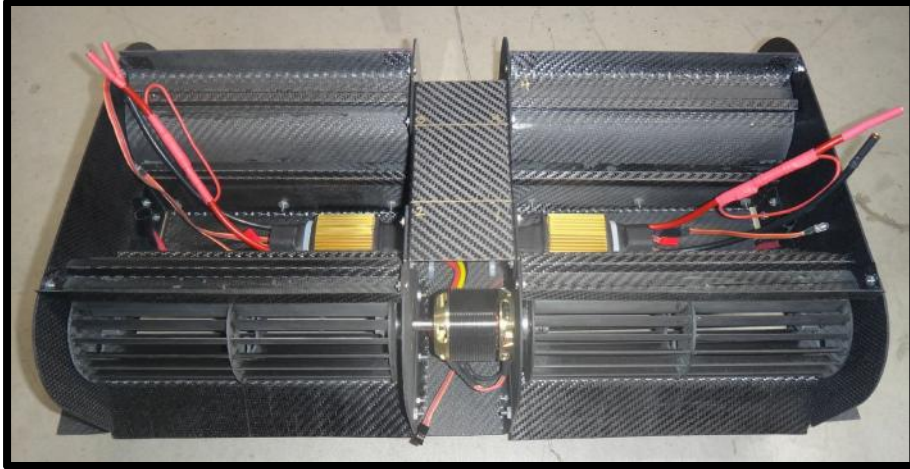


Figure 41. Assembled platform with four cross-flow fans and two motors.

C. PLATFORM TESTING

1. Experimental Setup

The motor controllers were placed above the platform and the batteries were mounted below the platform for better weight distribution. A set of cables connected the chassis to the control center. To ensure the safety of personnel as well as the integrity of the chassis and the control system, a line was run from each corner of the chassis to an anchoring block. A landing platform provided a larger space for flow and thrust generation during take-off and a cushion below ensured the well-being of the batteries upon landing.

2. Platform Control

The chassis' two Scorpion 4025 motors were powered by two lithium polymer batteries and controlled via two motor controllers and the two potentiometer setup in Figure 22. Each motor was controlled independently by its associated motor controller and potentiometer. A set of cables was run from the chassis to the potentiometer control center.

3. Platform Testing

The lines were attached to the blocks and the cables were connected from the motor controllers to the control center. Voltage measurements were taken and the chassis was ready for lift-off. To begin, both potentiometers were slowly dialed up and the chassis took flight as seen in Figure 42. The initial flight began unsteadily, but steadied after take-off and increasing rotor speed. After a successful first flight, two additional flights were conducted. Each flight lasted approximately 15 seconds. The second and third tests were much steadier because the initial speed was increased rapidly. Follow-on platform testing determined maximum thrust to be 7.40 kg, resulting in an effective thrust-to-weight ratio of 1.79.



Figure 42. Successful lift-off of four rotor chassis.

THIS PAGE INTENTIONALLY LEFT BLANK

VI. CONCLUSIONS AND RECOMMENDATIONS

A. THRUST TO WEIGHT RATIO

Measurements demonstrated that for the first time, thrust-to-weight ratios of greater than 1.0 could be realized using cross-flow fan propulsion for vertical take-off. This requires high speeds and low weights. The Scorpion 4025 motor allowed the cross-flow fan to achieve a thrust-to-weight ratio of 1.187 at a mere 7,000 rpm. This was very promising and led to the design of the test platform.

B. HOUSING AND ROTOR DESIGN

A new 20-bladed cross-flow fan was successfully designed, analyzed and tested to verify its thrust and power consumption characteristics. While the 78 mm, 20-bladed cross-flow fan and housing unit did produce a much larger thrust than its 16-bladed counterpart, it may not be the most efficient assembly. Simulations conducted using the laminar flow model demonstrated a large amount of flow back into the outlet. This indicated that there may be a better housing design for the 20-bladed cross-flow fan.

C. PLATFORM DESIGN

The initial platform design successfully demonstrated VTOL and resulted in a thrust-to-weight ratio of 1.79. Although this platform was successful, there is much work ahead. The current chassis design is limited by its tether. It would be optimum to have a remote control system in place to operate the platform independently. Additionally, individual motor control for each rotor would be optimum. Not only would this prevent the loss of one motor depowering two rotors, but it would also allow for better directional control of the platform.

D. RECOMMENDATIONS

Once vertical take-off is achieved and transition to horizontal flight occurs, the cross-flow fan can be operated more efficiently, which would reduce the power and increase range. Designing a system capable of sustained operation will be the only way

to make vertical take-off and landing with cross-flow-fan propulsion a reality. The key to this is determining the optimum power system and cross-flow-fan design.

To determine the most efficient power system, an investigation of additional motors and batteries should be conducted through coordination with electrical engineering personnel. Similarly, control systems engineering personnel should be consulted on a more efficient remote control system.

Higher values of thrust may be achieved by orienting the cross-flow-fan assembly at an angle to account for the velocity vectors. Additionally, the shape of the outlet could be redesigned to decrease the amount of back-flow and increase efficiency. One means of streamlining the fabrication process would be to attach the housings to the endplates via a groove. This would allow for more consistent cross-flow fan production.

As the test platform becomes more complex, it will be necessary to re-design the platform to maintain a thrust-to-weight ratio greater than 1.0. This could be accomplished by optimizing the spacing and location of the components on the chassis as well as removing unnecessary material.

There are many ways of improving the design process. Research should be streamlined into a more iterative process for determining number of blades, blade size, and positioning. Delagranges' [14] experimental work revealed that a dip in thrust occurred in the vicinity of the central rotor support disk and Martin's simulations [18] with a 30-bladed 101.6 mm fan determined that utilizing a smaller time-step resulted in a 5.5 percent increase in thrust and an 8.2 percent increase in power. Combined research indicates that a 3-dimensional simulation with half-degree time-steps should be analyzed in ANSYS-CFX. Additionally, the shear stress transport model should be used to determine the most accurate fluid model for simulation.

APPENDIX A. ANSYS-CFX SETTINGS AT 9,000 RPM

MESH REPORT		
Domain	Nodes	Elements
Housing Domain	475,196	234,800
Rotor Domain	375,536	183,722
All Domains	850,732	418,522

DOMAIN PHYSICS	
Domain—Housing Domain	
Type	Fluid
Location	B104
Materials	
Air Ideal Gas	
Fluid Definition	Material Library
Morphology	Continuous Fluid
Settings	
Buoyancy Model	Non Buoyant
Domain Motion	Stationary
Reference Pressure	1.0000e+00 [atm]
Heat Transfer Model	Total Energy
Include Viscous Work Term	On
Turbulence Model	k epsilon
Turbulent Wall Functions	Scalable
High Speed Model	Off

DOMAIN PHYSICS	
Domain—Rotor Domain	
Type	Fluid
Location	B48
Materials	
Air Ideal Gas	
Fluid Definition	Material Library
Morphology	Continuous Fluid
Settings	
Buoyancy Model	Non Buoyant
Domain Motion	Rotating
Angular Velocity	9.0000e+03 [rev min ⁻¹]
Axis Definition	Coordinate Axis
Rotation Axis	Coord 0.3
Reference Pressure	1.0000e+00 [atm]
Heat Transfer Model	Total Energy
Include Viscous Work Term	On
Turbulence Model	k epsilon
Turbulent Wall Functions	Scalable
High Speed Model	Off

DOMAIN PHYSICS	
Domain Interface—Domain Interface 1	
Boundary List1	Domain Interface 1 Side 1
Boundary List2	Domain Interface 1 Side 2
Interface Type	Fluid Fluid
Settings	
Interface Models	General Connection
Frame Change	Transient Rotor Stator
Mass and Momentum	Conservative Interface Flux
Pitch Change	Automatic
Mesh Connection	GGI

BOUNDARY PHYSICS	
Rotor Domain	
Boundary—Domain Interface 1 Side 2	
Type	INTERFACE
Location	RotorInterface
Settings	
Heat Transfer	Conservative Interface Flux
Mass and Momentum	Conservative Interface Flux
Turbulence	Conservative Interface Flux
Boundary—RotorSym1	
Type	SYMMETRY
Location	RotorSym1
Settings	
Boundary—RotorSym2	
Type	SYMMETRY
Location	RotorSym2
Settings	
Boundary—Rotor Domain Default	
Type	WALL
Location	F51.48, F52.48, F54.48, F55.48, F56.48, F57.48, F58.48, F59.48, F60.48, F61.48, F62.48, F63.48, F64.48, F65.48, F66.48, F67.48, F68.48, F69.48, F70.48, F71.48
Settings	
Heat Transfer	Adiabatic
Mass and Momentum	No Slip Wall
Wall Roughness	Smooth Wall

BOUNDARY PHYSICS	
Housing Domain	
Boundaries	
Boundary—Domain Interface 1 Side 1	
Type	INTERFACE
Location	HousingInterface
Settings	
Heat Transfer	Conservative Interface Flux
Mass and Momentum	Conservative Interface Flux
Turbulence	Conservative Interface Flux
Boundary—Inlet	
Type	OPENING
Location	Inlet
Settings	

Flow Direction	Normal to Boundary Condition
Flow Regime	Subsonic
Heat Transfer	Static Temperature
Static Temperature	2.8815e+02 [K]
Mass and Momentum	Opening Pressure and Direction
Relative Pressure	0.0000e+00 [Pa]
Turbulence	Medium Intensity and Eddy Viscosity Ratio
Boundary—Outlet	
Type	OUTLET
Location	Outlet
Settings	
Flow Regime	Subsonic
Mass and Momentum	Average Static Pressure
Pressure Profile Blend	5.00E-02
Relative Pressure	0.0000e+00 [Pa]
Pressure Averaging	Average Over Whole Outlet
Boundary—HousingSym1	
Type	SYMMETRY
Location	HousingSym1
Settings	
Boundary—HousingSym2	
Type	SYMMETRY
Location	HousingSym2
Settings	
Boundary—Housing Domain Default	
Type	WALL
Location	F106.104, F108.104, F111.104, F112.104, F114.104, F115.104, F116.104, F117.104
Settings	
Heat Transfer	Adiabatic
Mass and Momentum	No Slip Wall
Wall Roughness	Smooth Wall

THIS PAGE INTENTIONALLY LEFT BLANK

APPENDIX B. SCORPION MOTOR SPECIFICATIONS

Scorpion HKIII-4025-550KV (6mm)



Specifications

Stator Diameter	40 mm(1.57 in)
Stator Thickness	25 mm(0.98 in)
No. of Stator Arms	12
Magnet Poles	10
Motor Wind.	6T/7T Delta
Motor Wire	22-Strand 0.25mm
Motor Kv	550KV RPM/Volt
No-Load Current (I ₀ /10v).....	1.65 Amps
Motor Resistance (RM)	0.023 Ohms
Max Continuous Current	65 Amps
Max Continuous Power	2850 Watts
Weight	354 Grams (10.79 oz)
Outside Diameter	49.98 mm (1.97 in)
Shaft Diameter	5.98 mm (0.24 in)
Body Length	51.8 mm (2.04 in)
Overall Shaft Length	83.7 mm (3.30 in)
Max Lipo Cell	12s
Peak Current	90 Amps (5 seconds)
Peak Continuous Power	3900 Watts (5 seconds)
Motor Timing	5deg
Drive Frequency	8kHz

Scorpion HKIII-4035-560KV



Specifications

Stator Diameter.....	40 mm (1.57 in)
Stator Thickness.....	35 mm (1.024 in)
No. of Stator Arms.....	12
Magnet Poles.....	10
Motor Wind.....	8 Turn Delta
Motor Wire.....	23 - Strand 0.29mm
Motor Kv.....	560KV RPM / Volt
No-Load Current (IO).....	2.24 Amps @ 10v
Motor Resistance (RM).....	0.014 Ohms
Max Continuous Current.....	100 Amps
Max Continuous Power.....	4200 Watts
Weight.....	460 Grams (16.22 oz)
Outside Diameter.....	49.98 mm (1.97 in)
Shaft Diameter.....	5.98 mm (0.235 in)
Body Length.....	61.8 mm (2.43 in)
Overall Shaft Length.....	100.0 mm (3.93 in)
Max Lipo Cell.....	12s
Peak Current.....	120A (5 seconds)
Peak Power.....	5200 Watts (5 seconds)
Motor Timing.....	5deg
Drive Frequency.....	8kHz

Scorpion HK-5035-410KV (6mm Shaft)



Specifications

Stator Diameter	50 mm (1.56 in)
Stator Thickness	35 mm (1.37 in)
No. of Stator Arms	12
Magnet Poles	10
Motor Wind.	9 Turn Delta
Motor Wire	24-Strand 0.33 mm
Motor Kv	410KV RPM / Volt
No-Load Current (I ₀ /10V).....	2.12 Amps
Motor Resistance (R _m)	0.014 Ohms
Max Continuous Current.....	105 Amps
Max Continuous Power	5100 Watts
Weight	670 Grams (23.63 oz)
Outside Diameter	61.0 mm (2.4 in)
Shaft Diameter	5.98 mm (0.23 in)
Body Length	66.0 mm (2.59 in)
Overall Shaft Length	116.5 mm (4.59 in)
Max Lipo Cell	14s
Peak Current.....	145A (5 seconds)
Peal Power.....	7000 Watts (5 seconds)
Motor Timing	5deg
Drive Frequency	8kHz

THIS PAGE INTENTIONALLY LEFT BLANK

APPENDIX C. ANALYTICAL DATA

.2-mm SECTION 20-BLADED ROTOR								
SPEED		TORQUE	VELOCITY	MASS FLOW	POWER	THRUST		YPLUS
[rpm]	[Rad/s]	[Nm]	[ms ⁻¹]	[kgs ⁻¹]	[W]	[N]	[g]	[-]
4,000	418.879	0.000192	20.922	0.000186	0.080	0.003900	0.398	5.27974
6,000	628.319	0.000407	31.573	0.000273	0.256	0.008619	0.879	7.37778
8,000	837.758	0.000717	42.549	0.000362	0.601	0.015402	1.571	9.35232
9,000	942.478	0.000906	47.434	0.000394	0.853	0.018706	1.907	10.2787
9,500	994.838	0.000964	50.410	0.000417	0.959	0.020999	2.141	10.7758
10,000	1,047.198	0.001207	53.731	0.000451	1.264	0.024223	2.470	11.309

.2mm SECTION 20BLADE ROTOR W/O TURBULENCE MODELING							
SPEED		TORQUE	VELOCITY	MASS FLOW	POWER	THRUST	
[rpm]	[Rad/s]	[Nm]	[ms ⁻¹]	[kgs ⁻¹]	[W]	[N]	[g]
4,000	418.879	0.000234	23.141	0.000174	0.098	0.004027	0.411
6,000	628.319	0.000450	36.139	0.000249	0.283	0.008994	0.917
8,000	837.758	0.000769	46.234	0.000329	0.645	0.015222	1.552
9,000	942.478	0.001258	51.415	0.000383	1.185	0.019704	2.009
10,000	1047.198	0.001257	56.386	0.000414	1.316	0.023326	2.379

203-mm SECTION 20-BLADED ROTOR					
SPEED		TORQUE	POWER	THRUST	
[rpm]	[Rad/s]	[Nm]	[W]	[N]	[g]
4,000	418.879	0.192	80.307	3.902	397.846
6,000	628.319	0.408	256.113	8.623	879.312
8,000	837.758	0.718	601.323	15.41	1,571.343
9,000	942.478	0.906	853.909	18.715	1,908.411
9,500	994.838	0.965	959.901	21.01	2,142.374
10,000	1,047.198	1.207	1,264.390	24.235	2,471.284

203-mm SECTION 20BLADE ROTOR W/O TURBULENCE MODELING					
SPEED		TORQUE	POWER	THRUST	
[rpm]	[Rad/s]	[Nm]	[W]	[N]	[g]
4,000	418.879	0.238	99.606	4.087178727	416.7762413
6,000	628.319	0.457	286.882	9.128970768	930.89595
8,000	837.758	0.781	654.271	15.45005148	1575.466799
9,000	942.478	1.276	1203.001	19.99996557	2039.428915
10,000	1047.198	1.276	1335.870	23.6754447	2414.223481

THIS PAGE INTENTIONALLY LEFT BLANK

APPENDIX D. ANSYS-CFX FLOW FIELDS AT ALL SPEEDS

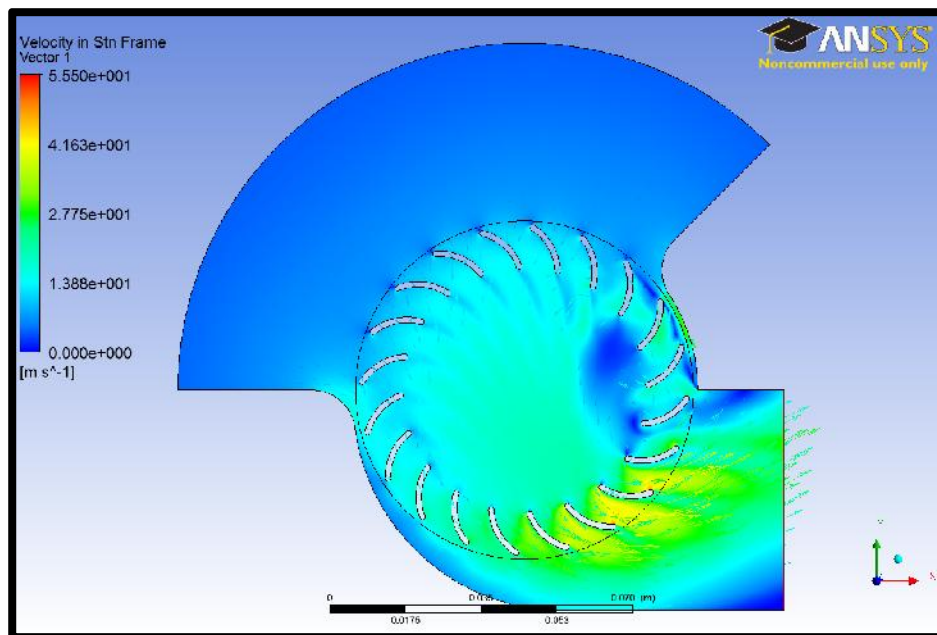


Figure 43. Flow Field at 4,000 rpm with the k-epsilon turbulence model.

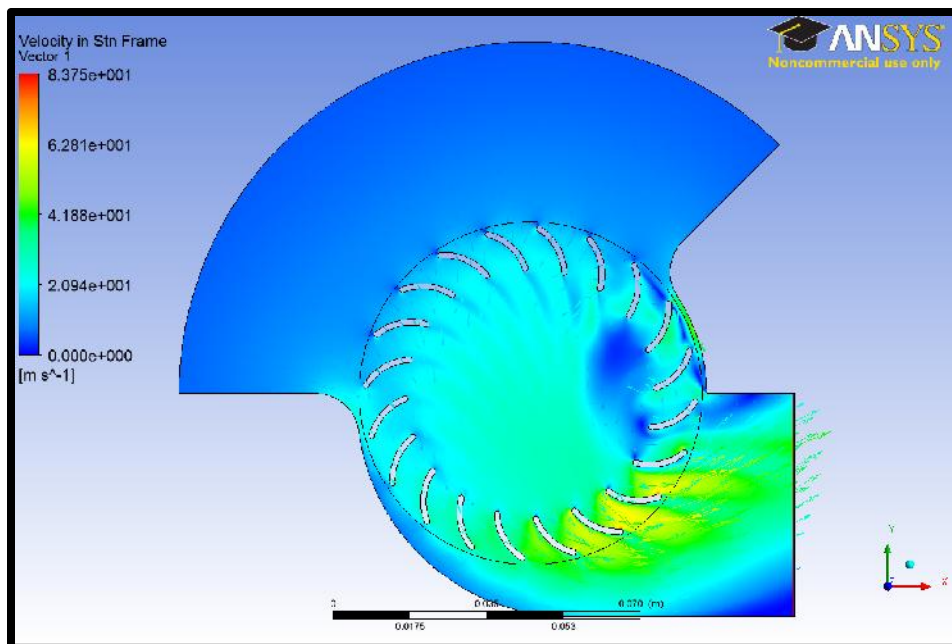


Figure 44. Flow Field at 6,000 rpm with the k-epsilon turbulence model.

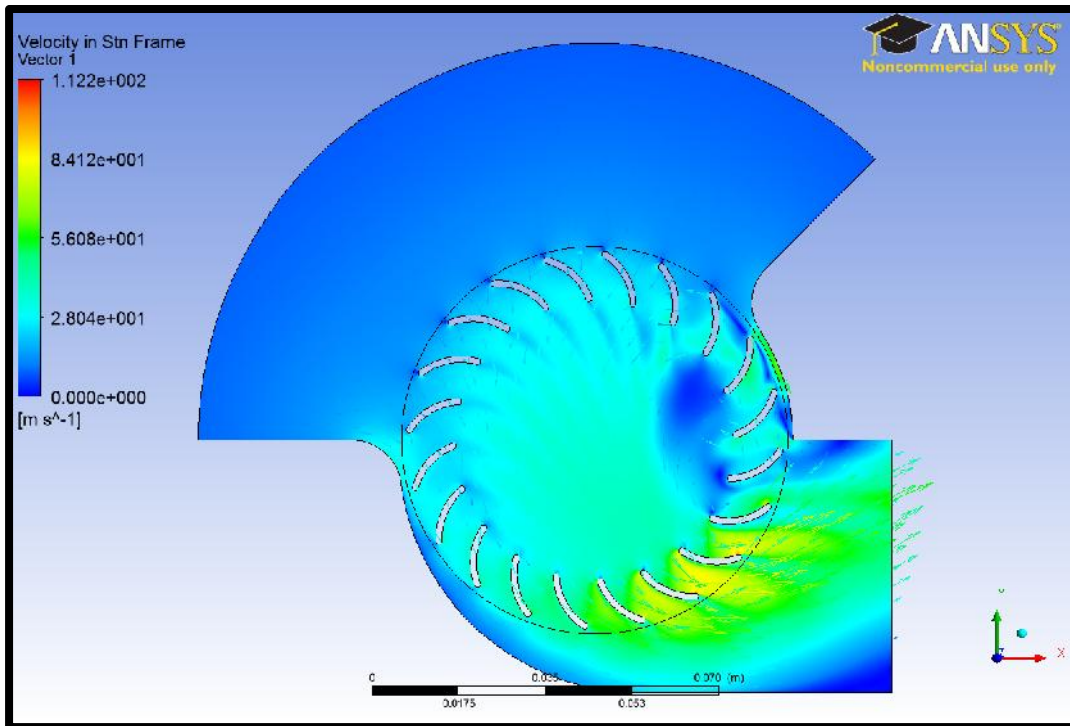


Figure 45. Flow Field at 8,000 rpm with the k-epsilon turbulence model.

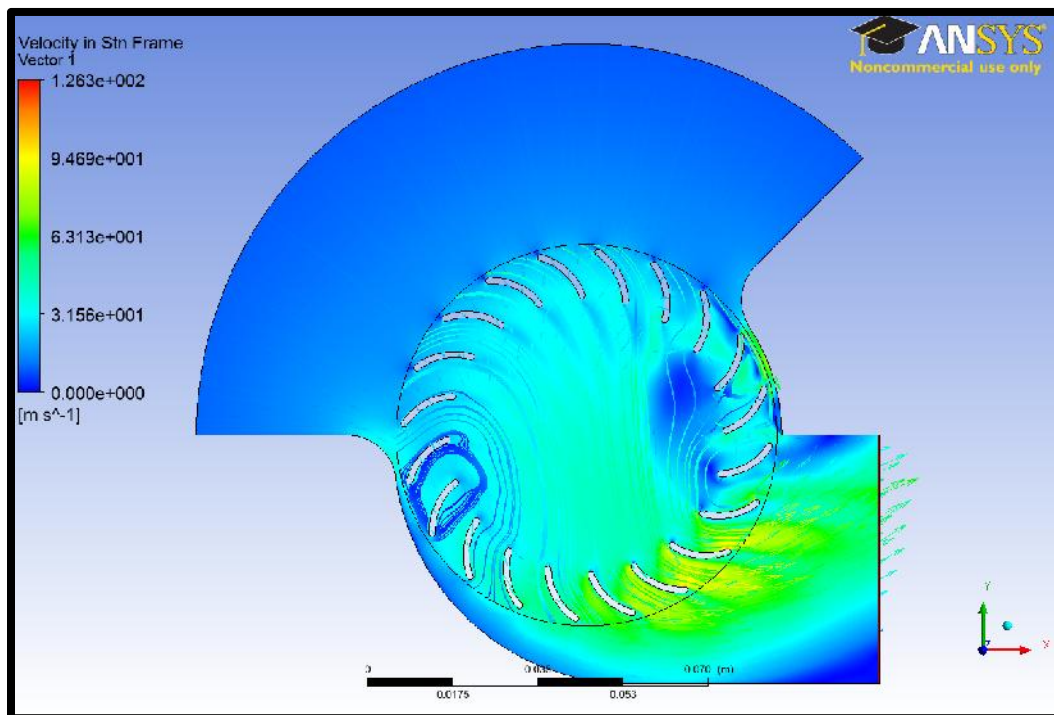


Figure 46. Flow Field at 9,000 rpm with the k-epsilon turbulence model.

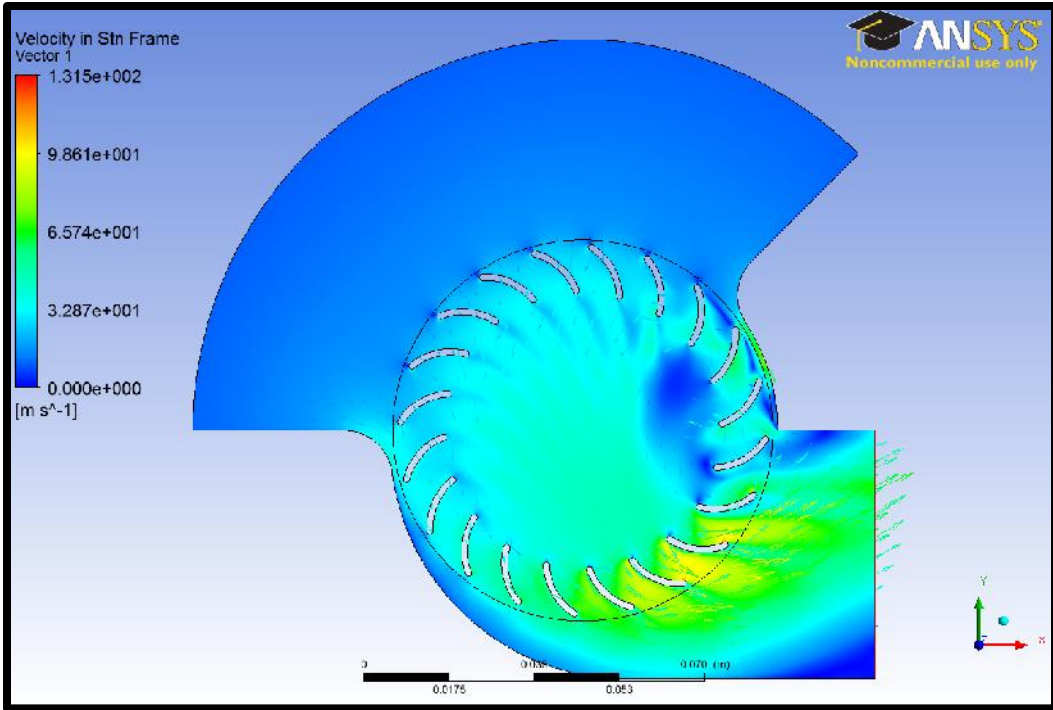


Figure 47. Flow Field at 9,500 rpm with the k-epsilon turbulence model.

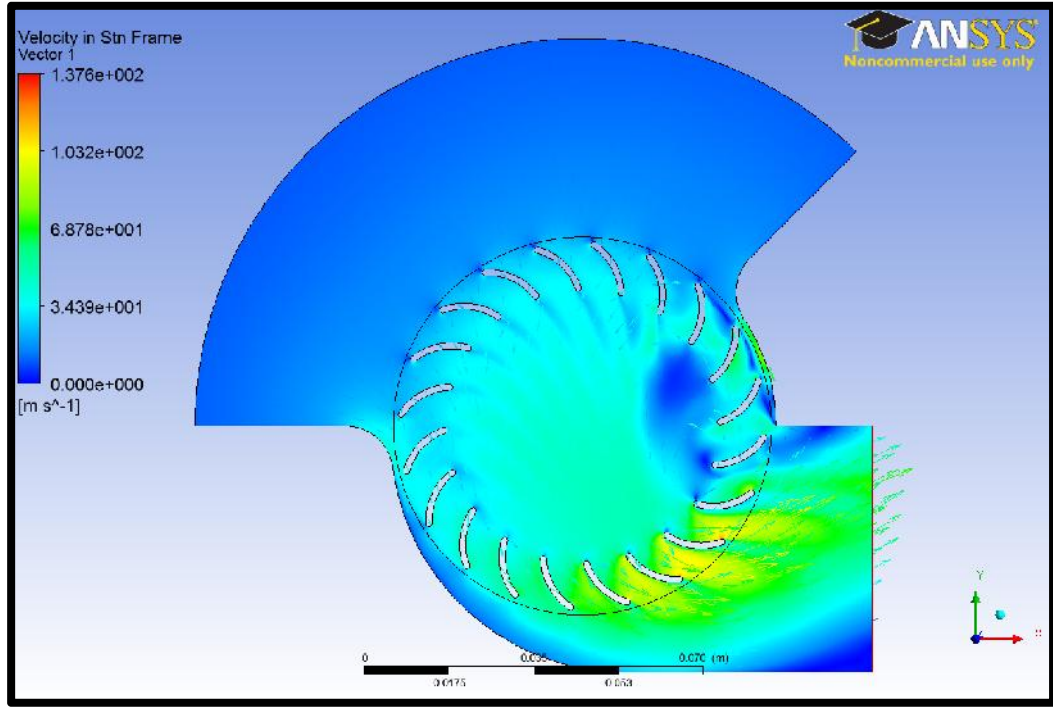


Figure 48. Flow Field at 10,000 rpm with the k-epsilon turbulence model.

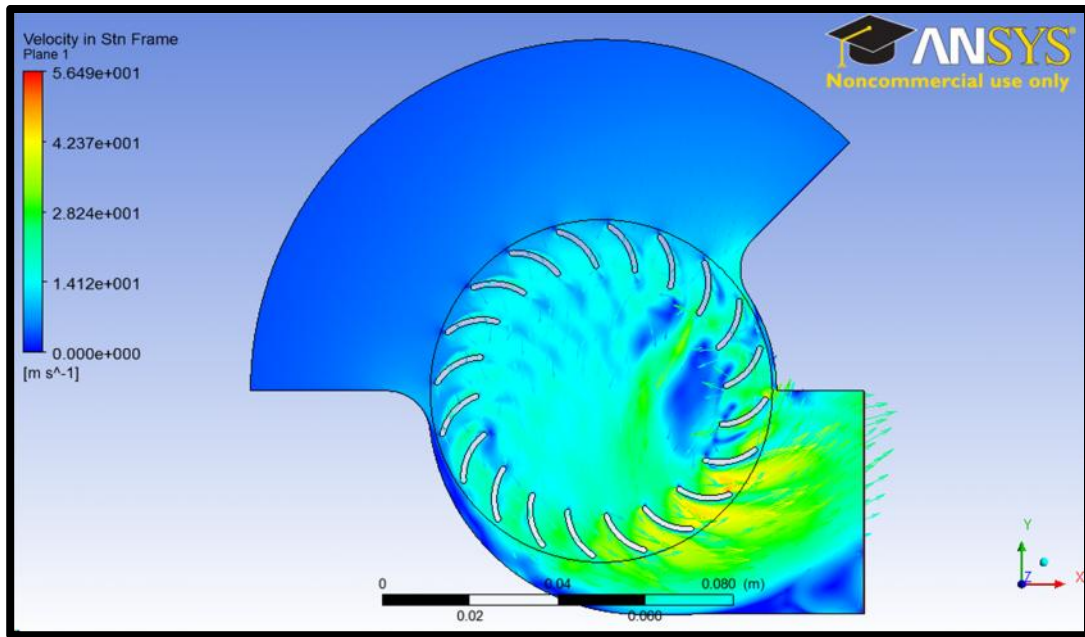


Figure 49. Laminar flow field at 4,000 rpm.

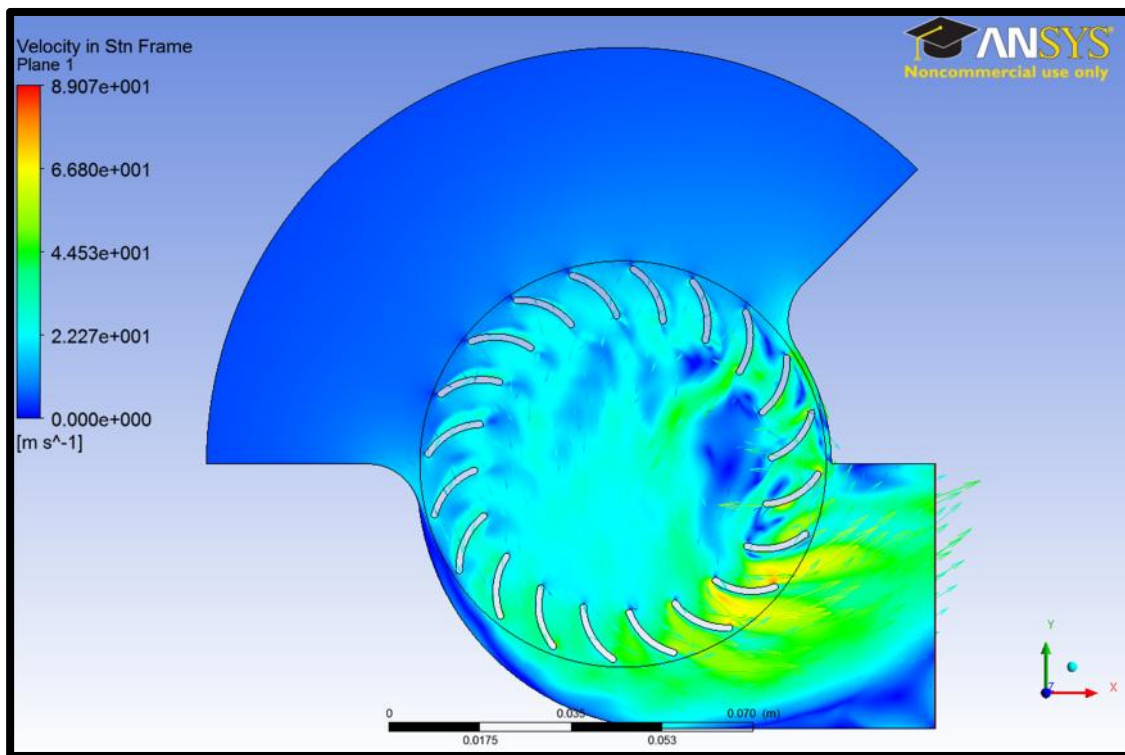


Figure 50. Laminar flow field at 6,000 rpm.

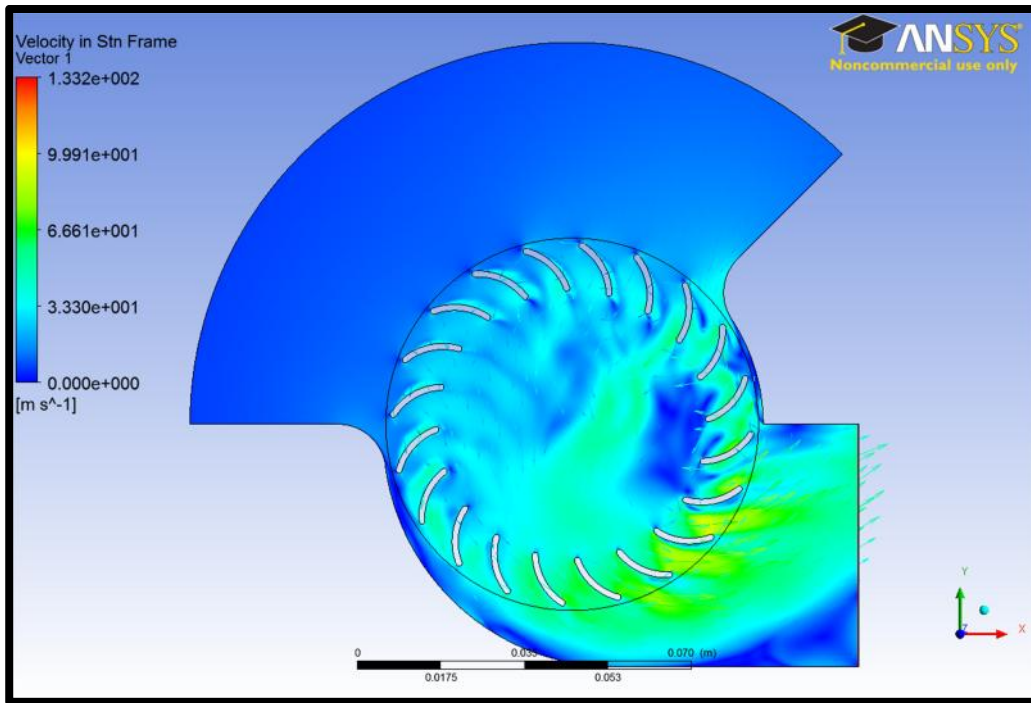


Figure 51. Laminar flow field at 8,000 rpm.

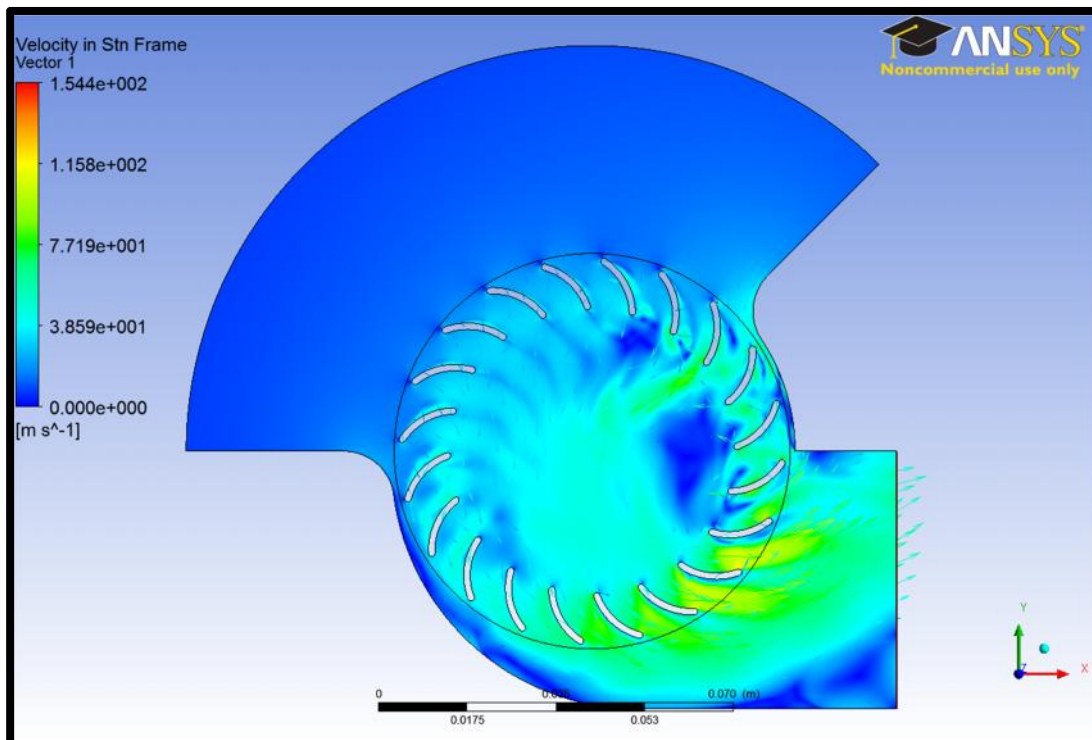


Figure 52. Laminar flow field at 9,000 rpm.

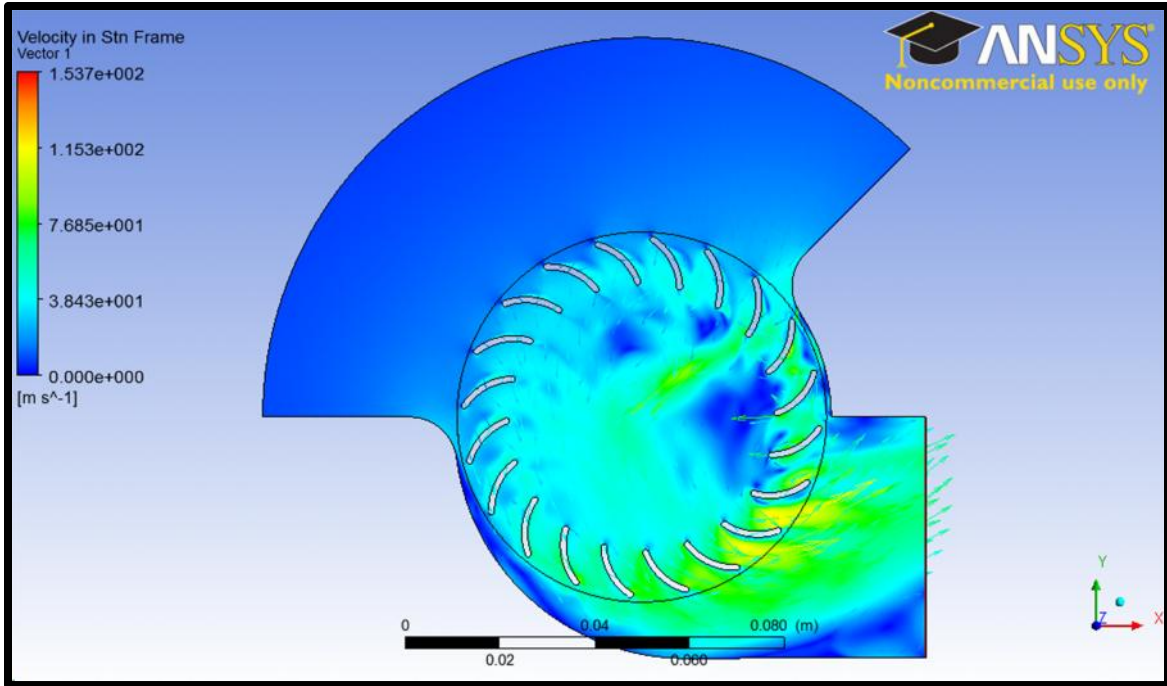


Figure 53. Laminar flow field at 10,000 rpm.

APPENDIX E. ANSYS-CFX STREAM LINES AT ALL SPEEDS

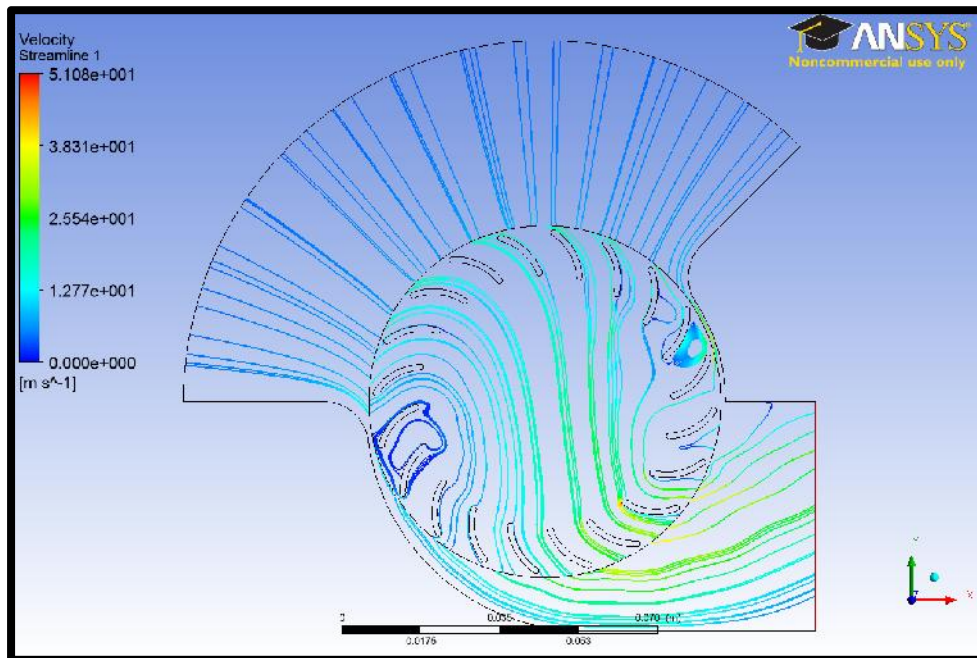


Figure 54. Streamlines at 4,000 rpm with the k-epsilon turbulence model.

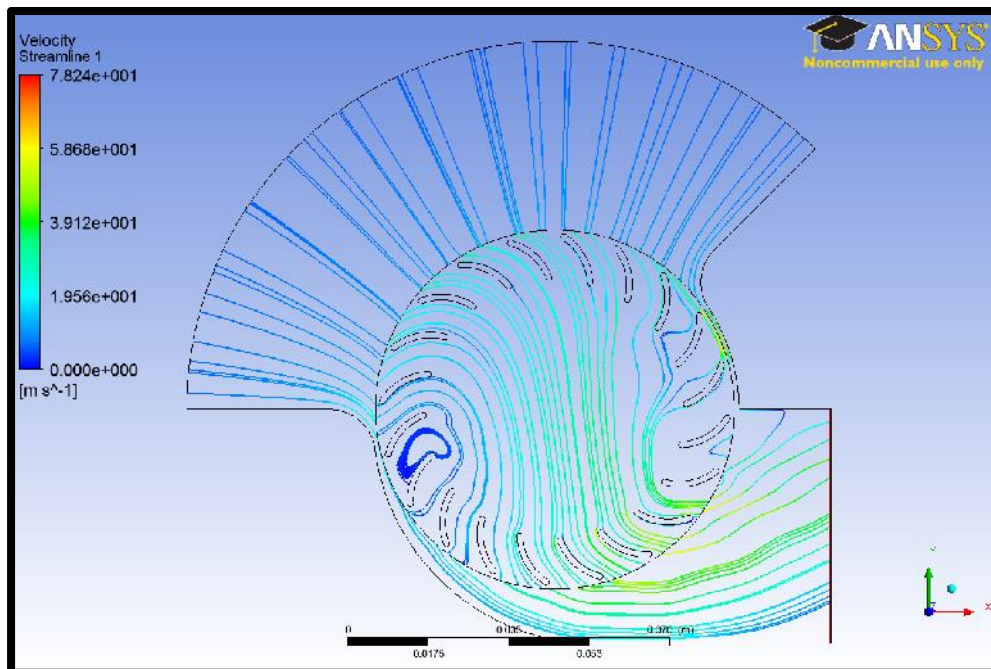


Figure 55. Streamlines at 6,000 rpm with the k-epsilon turbulence model.

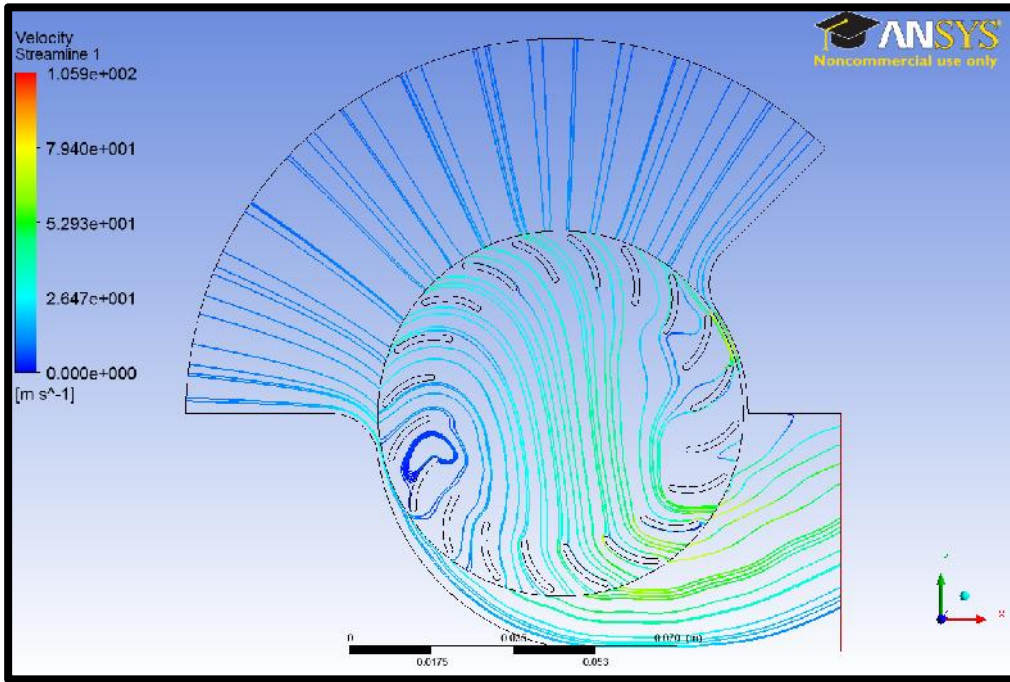


Figure 56. Streamlines at 8,000 rpm with the k-epsilon turbulence model.

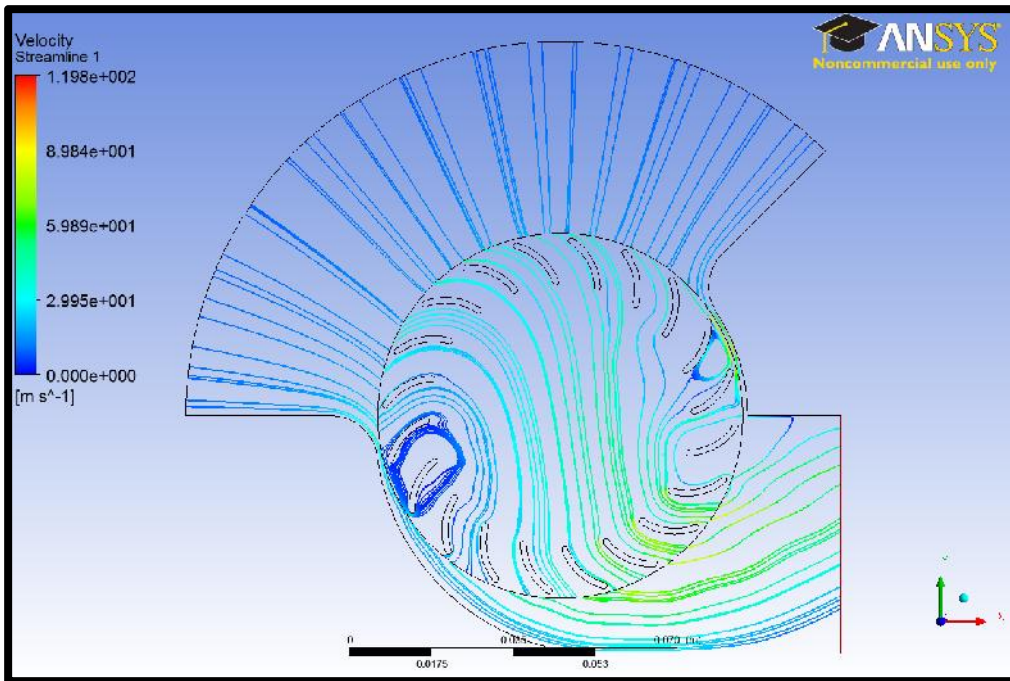


Figure 57. Streamlines at 9,000 rpm with the k-epsilon turbulence model.

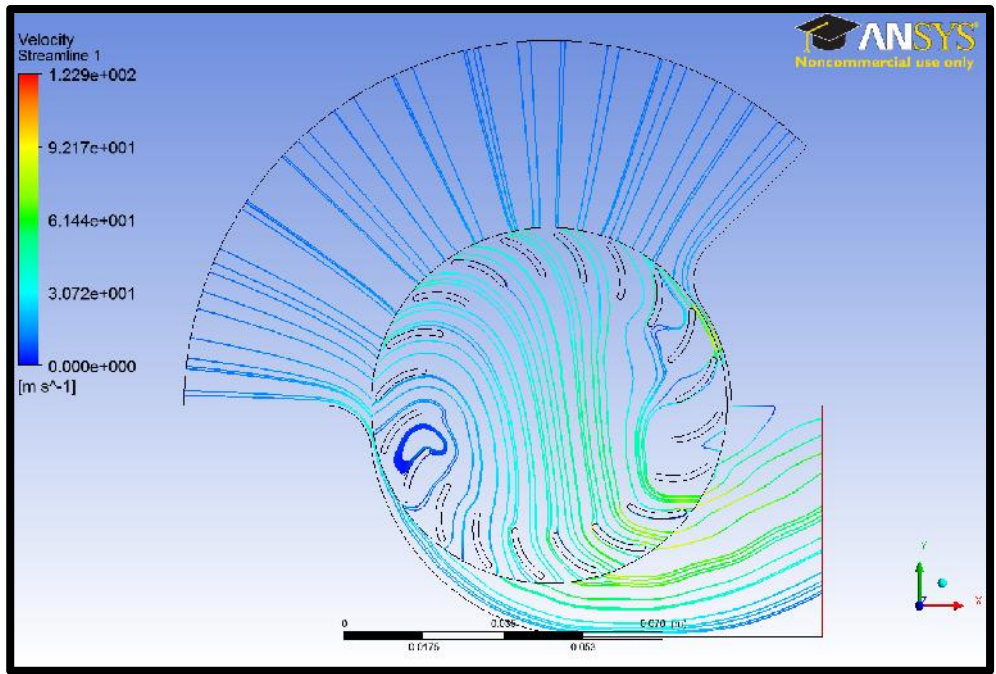


Figure 58. Streamlines at 9,500 rpm with the k-epsilon turbulence model.

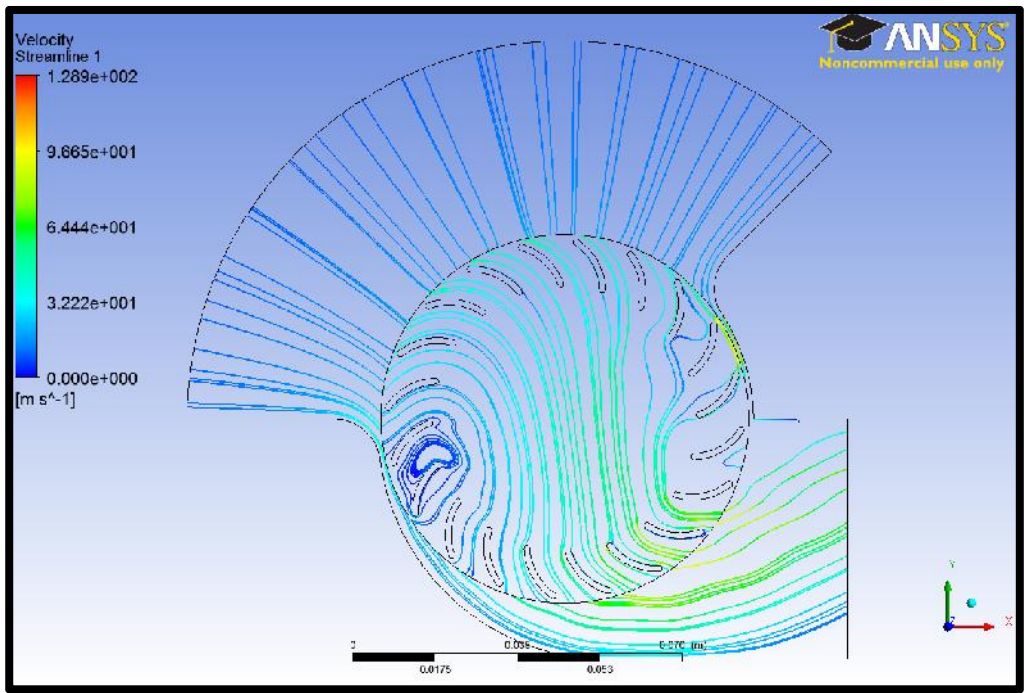


Figure 59. Streamlines at 10,000 rpm with the k-epsilon turbulence model.

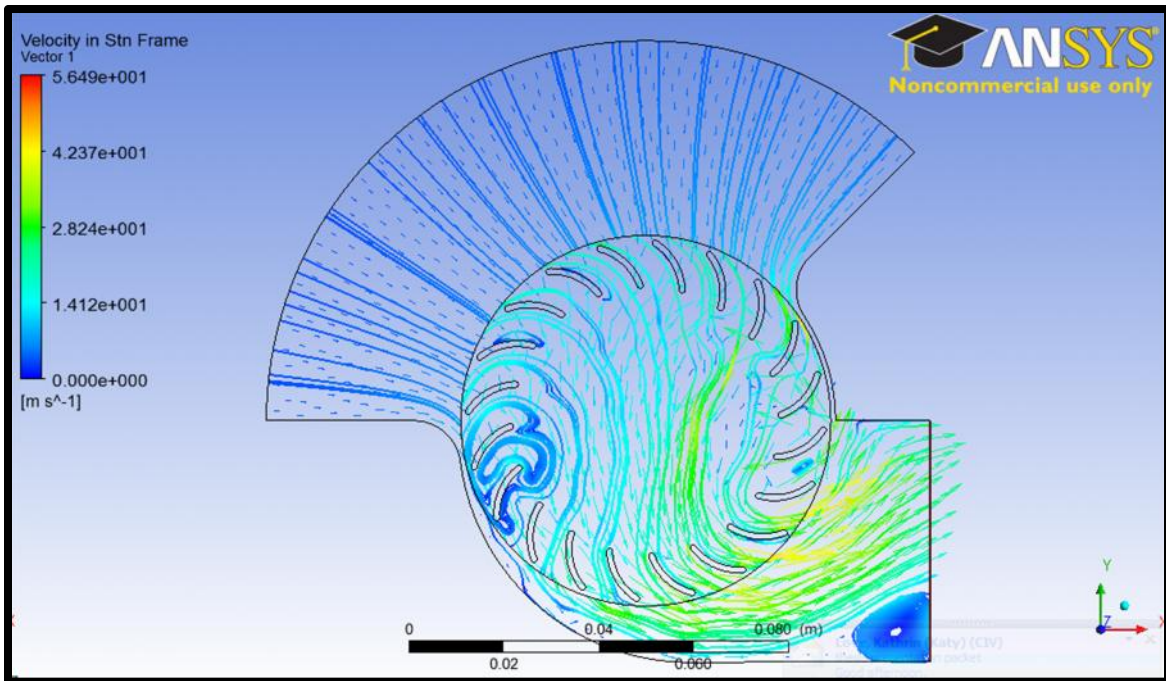


Figure 60. Laminar flow streamlines at 4,000 rpm.

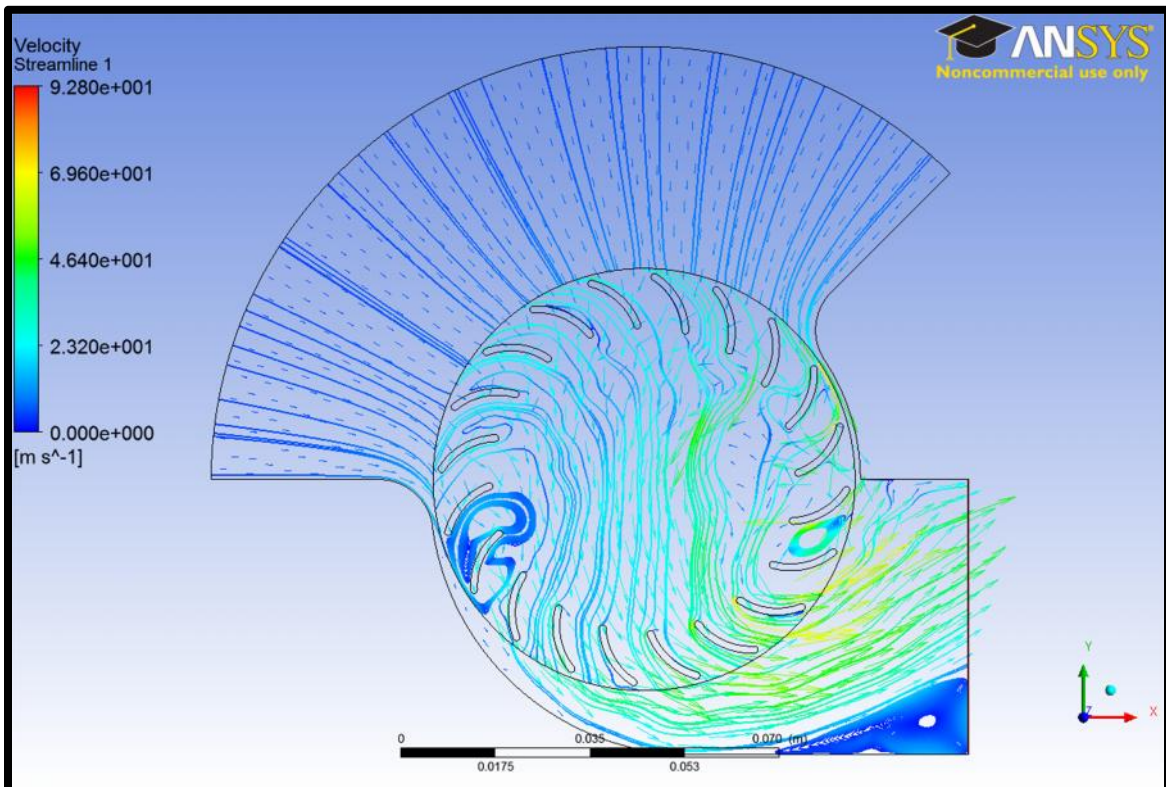


Figure 61. Laminar flow streamlines at 6,000 rpm.

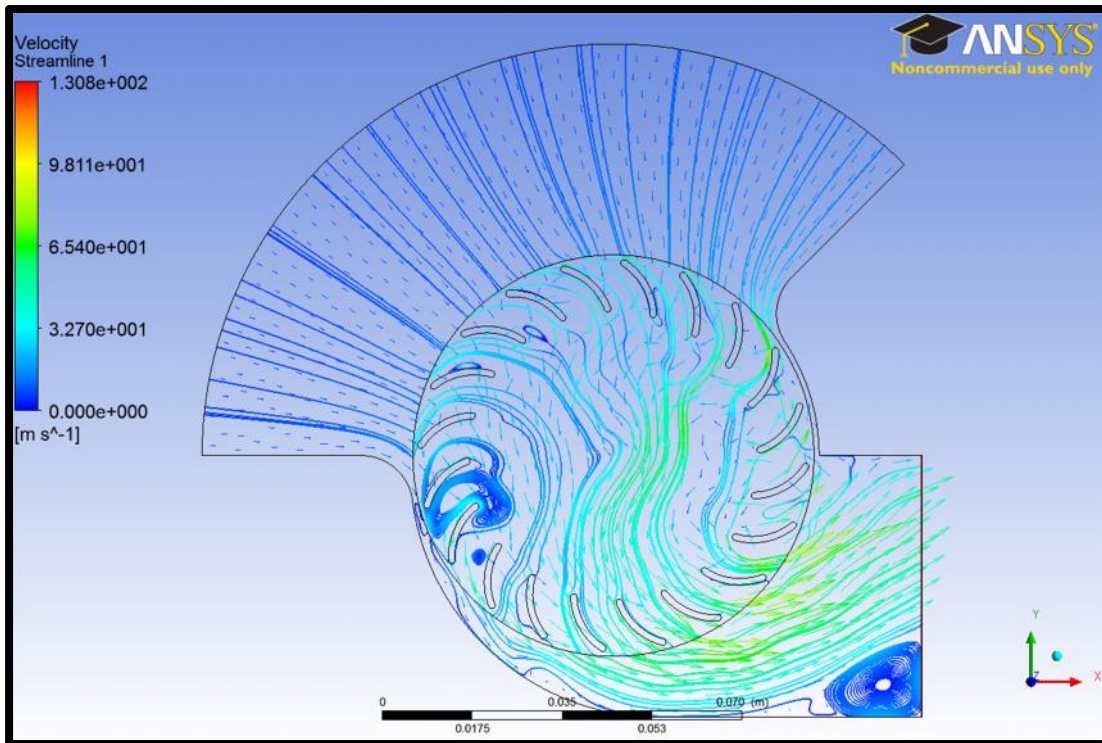


Figure 62. Laminar flow streamlines at 8,000 rpm.

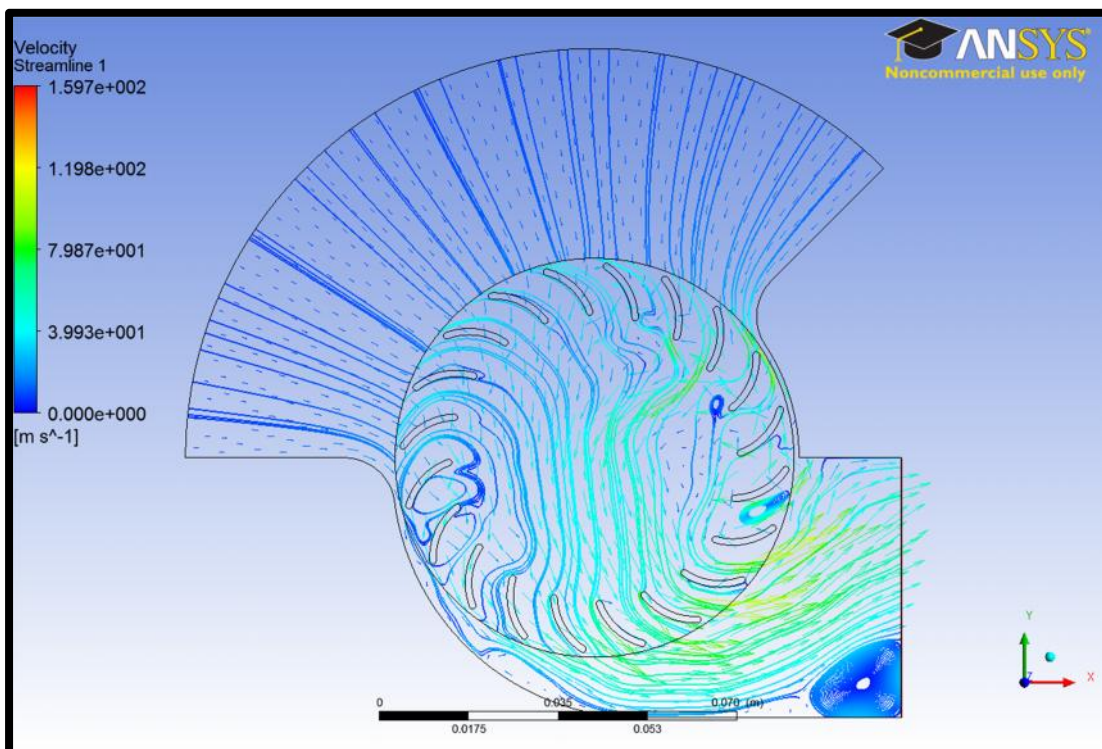


Figure 63. Laminar flow streamlines at 9,000 rpm.

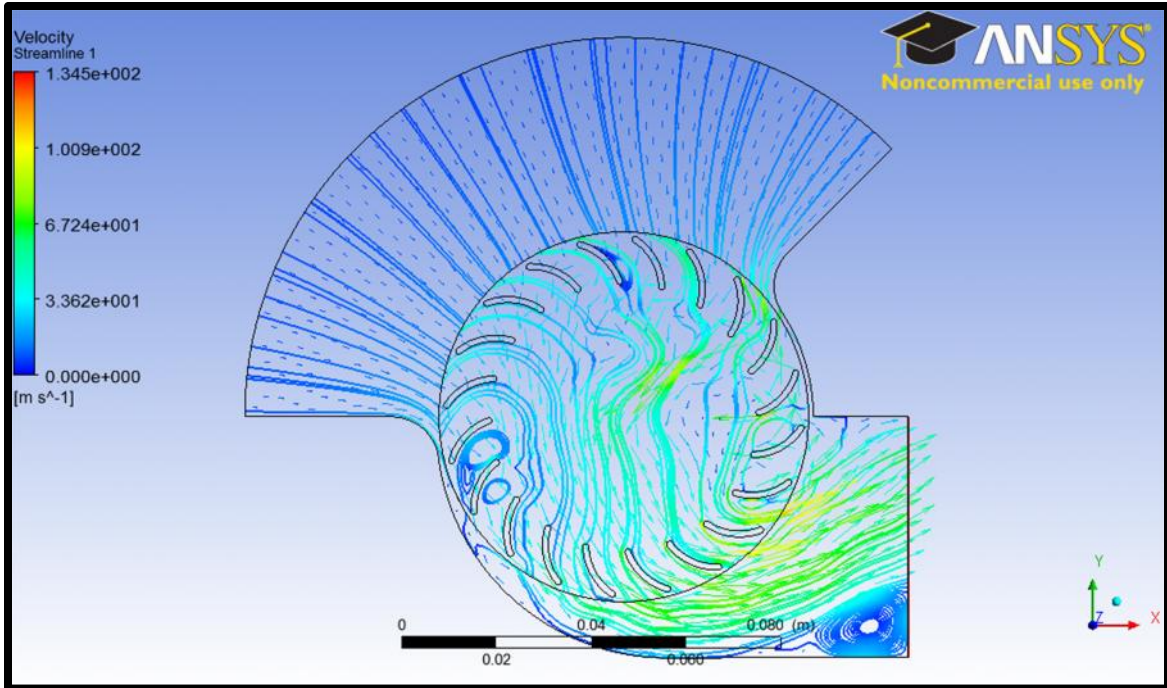


Figure 64. Laminar flow streamlines at 10,000 rpm.

APPENDIX F. EXPERIMENTAL TEST DATA

4025 MOTOR							4035 MOTOR		5035 MOTOR	
SPEED	THRUST	THRUST	THRUST	CURRENT	VOLTAGE	POWER	SPEED	THRUST	SPEED	THRUST
[rpm]	[g]	[g]	[g]	[A]	[V]	[W]	[rpm]	[g]	[rpm]	[g]
4,000	477	495	434	7.1	23.32	165.572	4,000	-	4,000	-
6,000	1,025	1,160	1,044	23.9	23.45	560.455	6,000	-	6,000	-
7,000	-	-	-	-	-	-	7,000	1,369	7,000	-
8,000	1800	2,100	1,886	65.9	23.82	1,569.738	8,000	1,800	8,000	-
8,500	2,000	-	-	-	-	-	8,500	-	8,500	2,050
8,700	2,200	-	-	-	-	-	8,700	-	8,700	-
8,800	2,550	-	-	88.6	23.82	2,110.452	8,800	-	8,800	-
9,000	2,295	-	-	-	-	-	9,000	2,300	9,000	-
9,400	-	-	-	-	-	-	9,400	2,544	9,400	-
9,500	-	-	-	-	-	-	9,500	2,544	9,500	-
9,700	-	-	-	-	-	-	9,700	2,730	9,700	-

ROUTER SETUP				
SPEED	THRUST	CURRENT	VOLTAGE	POWER
[rpm]	[g]	[A]	[V]	[W]
4,000	490	7.5	41	307.5
6,000	1180	13.27	61	809.47
7,000	1590	16.62	72	1196.64
8,000	2130	20.6	84	1730.4
9,000	2650	24.1	97	2337.7

THIS PAGE INTENTIONALLY LEFT BLANK

LIST OF REFERENCES

- [1] Mortier, Paul. "United States Patent Office No.: US 1893/507445," October 24, 1893.
- [2] Naval Air System Command contract N00019-74-C-0434, *Multi-Bypass Ratio Propulsion System Technology Development*, Vol. I-III, Vought Systems Division, LTV Aerospace Corporation, July 24, 1975.
- [3] G. J. Harloff, "Cross-flow fan experimental development and finite-element modeling," Ph.D. dissertation, University of Texas at Arlington, Arlington, Texas, 1979.
- [4] K. Chawla, "Optimization of cross flow fan housing for airplane wing installation," M.S. thesis, Department of Mechanical Engineering, University of Texas at Arlington, Arlington, Texas, 1984.
- [5] C. H. Lin, "A wind tunnel investigation of the external aerodynamics of an airfoil with an internal cross flow fan," M.S. thesis, Department of Mechanical Engineering, University of Texas at Arlington, Arlington, Texas, 1984.
- [6] T. W. Nieh, "The propulsive characteristics of a cross flow fan installed in an airfoil," M.S. thesis, Department of Mechanical Engineering, University of Texas at Arlington, Arlington, Texas, 1988.
- [7] D. H. Gossett, "Investigation of cross flow fan propulsion for a lightweight VTOL aircraft," M.S. thesis, Department of Aeronautics and Astronautics, Naval Postgraduate School, Monterey, California, March 2000.
- [8] W. T. Cheng, "Experimental and numerical analysis of a crossflow fan," M.S. thesis, Department of Aeronautics and Astronautics, Naval Postgraduate School, Monterey, California, December 2003.
- [9] C. W. Schreiber, "Effect of span variation on the performance of a cross flow fan," M.S. thesis, Department of Mechanical and Astronautical Engineering, Naval Postgraduate School, Monterey, California, June 2006.
- [10] J. M. Ulvin, "Experimental investigation of a six inch diameter, four inch span cross-flow fan ," M.S. thesis, Department of Mechanical and Astronautical Engineering, Naval Postgraduate School, Monterey, California, June 2008.
- [11] V. Antoniadis, "Numerical and experimental investigation of performance improvements of a cross-flow fan ," M.S. thesis, Department of Mechanical and Aerospace Engineering, Naval Postgraduate School, Monterey, California, June 2010.

- [12] J. Kummer, 2007, "Propulsive wing." [Online]. Available: <http://www.propulsivewing.com>
- [13] Kummer, Joseph, Allred, Jimmie. "United States Patent Application Publication No.: US 2012/0111994 A1," 10 May 2012.
- [14] C. Delagrangé, "Viability of cross-flow fan for vertical take-off and landing aircraft," M.S. thesis, Department of Mechanical and Aerospace Engineering, Naval Postgraduate School, Monterey, California, June 2012.
- [15] I. Yeo, "Thrust augmentation study of cross-flow fan for vertical take-off and landing aircraft," M.S. thesis, Department of Mechanical and Aerospace Engineering, Naval Postgraduate School, Monterey, California, September 2012.
- [16] H. T. Yu, "Experimental investigation and numerical prediction of a cross-flow fan," M.S. thesis, Department of Mechanical and Astronautical Engineering, Naval Postgraduate School, Monterey, California, December 2006.
- [17] G. Gansen, 2007, "Scorpion Power Systems," [Online], Available: <http://www.scorpionsystem.com>
- [18] M. J. Martin, "Designing a cross-flow fan rotor for vertical take-off and landing aircraft," M.S. thesis, Department of Mechanical and Aerospace Engineering, Naval Postgraduate School, Monterey, California, June 2013.

INITIAL DISTRIBUTION LIST

1. Defense Technical Information Center
Ft. Belvoir, Virginia
2. Dudley Knox Library
Naval Postgraduate School
Monterey, California